THE ASTROPHYSICAL JOURNAL, 437:802–826, 1994 December 20

OPTICALLY THICK WINDS IN NOVA OUTBURSTS

MARIKO KATO
Department of Astronomy, Keio University, Hiyoshi, Kouhoku-ku, Yokohama 223, Japan;
mariko@educ.cc.keio.ac.jp

AND

IZUMI HACHISU
Department of Earth Science and Astronomy, College of Arts and Sciences, University of Tokyo, Komaba, Meguro-ku, Tokyo 153, Japan;
hachisu@kyohou.c.u-tokyo.ac.jp
Received 1994 February 7; accepted 1994 June 28

ABSTRACT

Using the OPAL opacity, we have calculated a seqence of optically thick wind solutions, which mimics a time-dependent evolution of the decay phase of novae. Strong winds are driven by a large peak in the OPAL opacity and, as a result, theoretical timescale of nova duration is drastically shortened compared with the use of the old opacity. Thus, we are able to resolve a theoretical problem of nova duration: the theoretical timescale of nuclear burning for the initial envelope mass at ignition is too long to reconcile with the observational durations of novae.

Good quality light curves are automatically obtained from the combination of the optically thick wind theory and the OPAL opacity. We have compared our theoretical light curves with the observations of a well-studied classical nova, Nova Cygni 1978, and found that our 1.0 $M_\odot$ white dwarf model shows an excellent agreement with the observations both for the visual light curves and for the ultraviolet light curves and also for the expansion velocities of the envelope. These results strongly suggest the validity of our steady state approach and indicate that the optically thick wind really occurs on the white dwarf at least in the decay phase of the nova. In other words, optically thick winds, in which the matter is accelerated deep inside the photosphere, are the main acceleration mechanism in the decay phase of novae. Comparison of our theoretical light curves with observational ones enables us to determine the mass of the white dwarf and the distance of the star. The distance to Nova Cygni 1978 is estimated to be 2.9–3.1 kpc with the white dwarf mass of 1.0 $M_\odot$. Thus, quantitative studies of light curve fitting will be able to provide/add useful information of binary parameters that have been poorly known.

The effects of the drag luminosity in the common envelope phase have also been estimated by a one-dimensional (spherical) model. It is found that the drag luminosity is as small as or smaller than 1% of the photospheric luminosity because the density of the envelope drops sharply near/outside the accelerating region of wind. Only for relatively low-mass white dwarfs, the decline rate of the light curves is much affected by the effects of a companion, for example, the decline rate of a 0.6 $M_\odot$ white dwarf and a 0.2 $M_\odot$ companion shows a similar rate of 0.7 $M_\odot$ without a companion. However, we may conclude that the accuracy of the mass determination of the white dwarf is still within 0.1 $M_\odot$.

Subject headings: novae, cataclysmic variables — stars: evolution — stars: individual (Nova Cygni 1978) — stars: interiors — stars: mass loss

1. INTRODUCTION

Nova have been widely accepted to be a thermonuclear runaway event on a white dwarf (Gallagher & Starrfield 1978; Starrfield 1989). During the outburst, an envelope on a white dwarf expands to a large size of $\sim 100\ R_\odot$ and a significant part of the envelope mass is ejected from the system. One of the most important questions remaining until now is what determines the nova duration and the speed class. The outburst of classical novae usually lasts from a few months to 1 year, that of slow novae lasts few tens of years, and that of recurrent novae from 10 days to several months (e.g., Payne-Gaposchkin 1957; Seitter 1990). On the other hand, thermonuclear runaway models yield too long durations of novae ($\gtrsim 10^3$ yr), which are simply derived from the timescale of nuclear burning for the envelope mass at ignition.

Several ideas have been proposed to reconcile the short nova duration and the long nuclear burning timescale: (1) a part of the envelope may be ejected at the first dynamical phase. (2) Wind mass loss may occur in the decay phase of novae. (3) Mass ejection may be accelerated by the drag luminosity due to the motion of a companion star in the common envelope phase of novae.

Many time-dependent calculations of nova outburst have been presented so far (e.g., Sparks, Starrfield, & Truran 1978; Prialnik, Shara, & Shaviv 1978; Nariai, Nomoto, & Sugimoto 1980; Prialnik 1986; Kato, Saio, & Hachisu 1989; Prialnik & Kovetz 1992, and references therein). Most of these works concern only very early stages of the outburst just after the hydrogen ignition and do not follow one or more cycles of novae. One of the reasons is that numerical difficulties in the extended envelope phase prevent us from continuing the calculation. Prialnik's work (1986) is one of a few exceptions. She followed a few cycles of nova. In her calculation, a part of the envelope matter is ejected by a shock wave at an early phase of the outburst, and then ejected by wind in the following phase. She was able to obtain a short t_3 time of 25 days for a massive

white dwarf of 1.25 $M_\odot$. Here, t_3 time is defined by the time that the visual magnitude drops by three from the peak luminosity. Such a strong mass loss is expected only on a massive white dwarf because shell flashes are too weak to eject a significant part of the envelope mass on less massive white dwarfs of $\lesssim 1.0\ M_\odot$. Thus, novae had ever been considered to occur on a relatively massive white dwarf such as $\gtrsim 1.2\ M_\odot$.

Nova outbursts have also been studied in a different approach, the steady state approach, where nova evolutions are followed by sequences of steady state envelope solutions on a white dwarf instead of a full time-dependent calculation. Since the pioneering work by Finzi & Wolf (1971) appeared, many works have followed it so far (e.g., Żytkow 1972, 1973; Ruggles & Bath 1979; Kato 1983b). Now we have an established way to follow the evolution of nova outburst by using a sequence of steady state solutions (Kato 1983b, 1985, 1991; Kato & Hachisu 1988). In this approach, we are able to treat mass loss from the system without unphysical treatments. The mass loss is automatically incorporated into the so-called continuum radiation driven wind, in which the acceleration occurs deep in the envelope (Friedjung 1966). This kind of wind is called *optically thick wind* because the matter is accelerated deep inside the photosphere.

The optically thick wind theory or method has an advantage that various physical values such as the wind mass-loss rate and the photosphere are accurately determined because, for example, the mass-loss rate is determined as an eigenvalue of the basic equations. As a result, we are able to obtain good quality light curves in the decay phase of novae as will be shown later. The recent results calculated by Kato & Hachisu (1988, 1989, and Table 1 of 1991b) show that the nova duration is as short as 1 year for a 1.3 $M_\odot$ and 30 years for a 0.9 $M_\odot$ white dwarf under the assumption of solar composition of nova envelope.

It has been believed that some of the recurrent novae are also a thermonuclear runaway event on a very massive white dwarf ($\gtrsim 1.3\ M_\odot$). Using the optically thick wind theory, Kato (1990a, b; 1991) calculated theoretical light curves of three recurrent novae, U Sco, RS Oph, and T Pyx. She fitted the theoretical light curves with the observational ones and to determine the white dwarf mass and the chemical composition of ejecta. The white dwarf mass is determined to be 1.38 $M_\odot$ for U Sco (Kato 1990a), 1.36 $M_\odot$ for RS Oph (Kato 1991), and $\sim 1.33\ M_\odot$ for T Pyx (Kato 1990b). Such high accuracies in the determination of the white dwarf mass come from the combination of the accurate light curves and the steep dependency of the decline rate of visual light curve on the white dwarf mass. However, she showed no light curves for other types of novae, neither classical novae nor slow novae.

Thus, the theoretical works told us that the observed short decay time of novae can be reproduced only for massive white dwarfs. This conclusion seems to be inconsistent with the observational aspect that most of the central stars of planetary nebulae and white dwarfs in binaries have mass as low as about 0.6 $M_\odot$ (Weidemann 1990). Truran & Livio (1986) and Ritter et al. (1991) tried to resolve this problem and concluded that more massive white dwarfs have a much shorter recurrence period and, as a result, a significant part of novae can be explained by explosions on very massive white dwarfs ($\gtrsim 1.2\ M_\odot$).

However, the advent of new opacities may change all of these pictures because a strong peak in the opacity has been reported at the temperature of $\log T(K) \sim 5.2$ (Iglesias, Rogers, & Wilson 1987, 1990; Iglesias & Rogers 1991, 1993; Rogers & Iglesias 1992). This peak in the new opacity is about 3 times larger than that of the Los Alamos opacity (Cox & Stewart 1970a, b; Cox, King, & Tabor 1973). Such a large enhancement of the new opacity certainly drives a strong wind in novae, because the acceleration of envelope matter is directly affected by the opacity value especially when the luminosity is very close to the Eddington luminosity as seen in nova envelopes (Kato & Iben 1992). It is, therefore, necessary to recalculate wind solutions and examine the effects of the new opacity.

A part of our recalculations has already been reported in Kato (1994). Her results clearly show that the decay timescale of novae is drastically shortened by the effects of the new opacity. Moreover, the shape of the theoretical light curve becomes so smooth that it can be directly fitted with the observational light curves. This is a remarkable progress in the sense that we are able to determine various physical parameters of novae by directly comparing the theoretical light curves with the observational ones. For example, we have succeeded in determining the mass of the white dwarf of a classical nova, Nova Cygni 1978. Simultaneous fitting of classical and ultraviolet (UV) light curves indicates the white dwarf mass of 1.0 $M_\odot$ and the distance of 3.0 ± 0.1 kpc to the star.

Moreover, the light curves for the other types of novae, slow novae and recurrent novae, can also be reproduced with the optically thick wind theory and the new opacity (Kato & Hachisu 1994). Thus, we are now able to construct good quality light curves for various kinds of novae. It also covers a wide range of evolutional timescale from very slow to fast novae. It should be noted that these are obtained unphysical treatments but with a single theory of the optically thick wind and the OPAL opacity. This suggests the plausibility of the strong peak of the new opacity, that is, it really exists! Good quality of the theoretical light curves will certainly open a new world to determine the physical parameters of novae such as the white dwarf mass and the distance to the star.

Our modeling of the optically thick wind does not include the effect of the companion star in nova system. The importance of the common envelope phase in nova systems has firstly been discussed by MacDonald (1980) for slow novae. The envelope on the white dwarf expands to a large size of $\sim 100\ R_\odot$ after the onset of nova outburst and, as a result, the companion star is engulfed by the expanding nova envelope because the orbit is usually $\sim 1\ R_\odot$ when the companion star is a zero age main-sequence star. The companion star moves supersonically in the nova envelope and there exists a friction between the envelope and the companion. He showed in his one-dimensional hydrodynamic calculation that the energy deposition into the envelope due to frictional processes causes rapid increase of the expansion velocity and visual magnitude. MacDonald, Fujimoto, & Truran (1985) examined the effects of the common envelope phase under the assumption of one-dimensional static polytropic envelope but for a wide range of white dwarf masses. They concluded that the drag luminosity is essentially important to shorten the nova duration. Their motivation was to resolve a theoretical problem that the nuclear burning time of the initial envelope mass is too long ($\gtrsim 10^3$ yr) compared with the observational ones (~ 10 yr).

Recent time-dependent calculations, however, showed the results against the MacDonald et al. (1985) conclusion. Livio et al. (1990) showed, in their two-dimensional adiabatic calculation of a 1.0 $M_\odot$ white dwarf and a 0.5 $M_\odot$ companion, that

the energy deposition due to the frictional processes quickly drops to a very small value of $\sim 50\,L_\odot$ because the density near the orbit decreases quickly. After the envelope settles down to a steady state, the drag luminosity is too small to affect the mass-loss rate. Their value of the mass-loss rate finally drops to $1 \times 10^{-6}\,M_\odot\,\mathrm{yr}^{-1}$, which is much smaller than the wind mass-loss rate obtained by Kato & Hachisu (1989) with the old opacity. Therefore, we may conclude that the drag luminosity is too small to affect the nova duration or the light curve.

The same conclusion that the drag luminosity is not effective can be derived from another time-dependent calculation by Shankar, Livio, & Truran (1991). They calculated common envelope evolution (in one-dimension) and concluded that the mass ejected from the system is increased by 8% (in their high-resolution calculation) and 67% (low-resolution calculation) by the effect of a companion. They defined the amount of matter ejected from the system by the condition that the velocity of matter exceeds the escape velocity calculated only from the white dwarf mass. It is interesting that if the gravity of the companion ($0.5\,M_\odot$) is included in the definition of escape velocity, their high-resolution model (in Fig. 6 of their paper) shows that the amount of mass ejected is exactly the same as that of the case without a companion. In their low resolutions calculation (95 zones), the velocity of the envelope matter jumps from zero to the escape velocity at the innermost one mesh (in Fig. 7 of their paper). It seems difficult to draw a definite conclusion from this calculation. Therefore, it is very unlikely that companion motion in common envelope contributes much of the acceleration of nova envelope matter.

It should be stressed that the gravity by the companion is important to correctly estimate the ejected mass. It works against the mass ejection. For example, the nova system mentioned above contains a $1.0\,M_\odot$ white dwarf and a $0.5\,M_\odot$ companion (zero age main-sequence) so that the escape velocity is increased by 22%. Kato & Hachisu (1991a, b) examined how effective is the drag luminosity including the gravity of a companion star within the framework of one-dimensional steady-state assumption. They found that the drag luminosity becomes as large as the diffusive luminosity only when the mass of white dwarf is as small as $0.6\,M_\odot$ or less, mainly because the envelope on more massive white dwarfs is too tenuous to generate large drag luminosity. However, wind mass loss does not occur on these low-mass white dwarfs, because it is suppressed by the additional gravity of companion. Moreover, the companion gravity increases the local Eddington luminosity and, as a result, the fractional energy generated by the companion can escape from the system by diffusion. So that the frictional heat does not directly accelerate the matter. It seems unlikely that the nova duration is much shortened by the presence of a companion. Thus, we cannot expect any drastic changes in nova evolution or nova duration only by the effect of a companion. However, we must still examine the effect of drag luminosity because the new opacity changes the envelope structure and, as a result, the light curves of low-mass white dwarfs may be affected by the presence of a companion. So we calculate several sequences of wind solutions including these effects.

The most important motivation of this paper is to fully describe the optically thick wind theory developed by us and its wide applicability to nova studies, because we have heard so many times groundless objections against the optically thick wind theory. For this reason, we try to dot our i's and cross our t's in writing this paper. It consists of several sections. We describe in § 2 the basic equations and the boundary conditions of the optically thick wind theory. Physical properties of wind solutions are shown in § 3 and also shown is the way how to make evolutional sequences from each steady state solution. A detailed case study of the light curve fitting is presented also in § 3 for Nova Cygni 1978. In § 4, effects of the OPAL opacity on steady state solutions and light curves are examined by comparing them with the previous works with the old opacity. The effects of the drag luminosity are discussed in § 5. Our assumptions in the present paper, that is, steady state assumption in the decay phase of novae, neglecting the convective energy transport, and neglecting the acceleration outside the photosphere, are examined in detail in § 6. The dependence of light curves on the chemical composition of nova envelope is also discussed in § 6. We summarize our results in § 7. Surface boundary conditions of wind mass loss solutions are described in detail in Appendix A. Since our numerical techniques are not popular in this field, we briefly explain the trapezoidal implicit method in Appendix B.

2. BASIC EQUATIONS OF OPTICALLY THICK WIND

2.1. *Optically Thick Wind Theory*

Figure 1 shows a schematic diagram of the evolutionary course of a nova outburst. Before the onset of a nova outburst, the accreting white dwarf stays at point A. When the envelope mass exceeds a critical value, unstable hydrogen burning ignites to trigger a nova outburst. The star brightens up and goes up in the H-R diagram. The hydrogen-rich envelope absorbs energy generated by nuclear reactions and expands to a large scale. Then the star moves redward. Mass loss begins at point B. At point C the envelope reaches a thermal equilibrium: the energy generated by nuclear burning balances with the energy lost from the photosphere. After the maximum expansion of the photospheric radius, the star moves blueward as the envelope mass decreases. A large part of the hydrogen-rich envelope has been lost until the mass loss stops at point D. Hydrogen shell burning still continues to point E and then the white dwarf gradually cools down to point A.

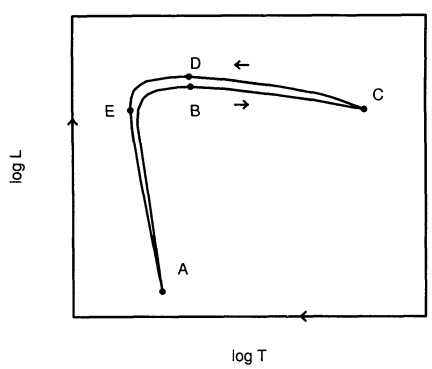

FIG. 1.—Schematic H-R diagram for an evolutionary track of one nova cycle. An accreting white dwarf stays at point A before the onset of hydrogen shell flash. After hydrogen ignites, the hydrogen-rich envelope on the white dwarf expands and wind mass loss begins at point B. The photospheric radius reaches its maximum value at point C. As the envelope mass decreases due to wind mass loss, the photosphere temperature increases and reaches point D where the wind mass loss stops. After that, the mass of the hydrogen-rich envelope gradually decreases due to hydrogen burning until the star reaches point E at which the nuclear burning vanishes. The star gradually cools down to point A.

Such an evolutionary path of a nova has been followed by time-dependent calculations with stellar-evolution code (e.g., Sparks et al. 1978; Nariai et al. 1980; Prialnik 1986). This method works well before and after the onset of the unstable hydrogen burning and also during the successive dynamical expanding stages (corresponding to the stages from point A to B). After the envelope expands greatly, however, some numerical difficulties prevent us from calculating nova evolution accurately. This kind of numerical difficulty are inherent in Henyey-type codes and no one succeeds in removing these difficulties from their codes. Instead, we adopted a different type of approach to follow the evolution of expanded nova envelopes.

In this expanded phase, the envelope is almost in a steady state, in which the energy generated by nuclear burning is balanced with the loss of energy radiated away from the photosphere. If steady state is assumed, we are able to follow the evolution further because we are free from the above numerical difficulties. Then the evolution of nova is followed by a sequence consisting of steady state (from point C to point D) and static (from D to A through E) envelope solutions. We believe that only this kind of approach enables us to compute the very expanded phase of novae.

Optically thick wind is a continuum-radiation driven wind in which the acceleration occurs deep inside the photosphere. Historically, the importance of radiation pressure in mass ejection of novae was suggested by Friedjung (1966). Such mass-losing envelope solutions were obtained first by Finzi & Wolf (1971) in relation to planetary nebula formation. Their solutions contain three free parameters because they did not impose boundary conditions. Ruggles & Bath (1979) constructed sequences consisting of steady wind solutions to follow nova evolution. Their inner bounary conditions, however, are not consistent with the energy generation by nuclear burning, that is, their inner boundary condition is inadequate.

Kato (1983b) firstly obtained consistent envelope solutions in thermal equilibrium and constructed sequences which follow the decay phase of novae. Surface boundary conditions were examined in detail by Kato (1985) to detect the occurrence of optically thick winds. Now, we have an established way to construct steady-state nova sequences. The method has been applied to the case of recurrent novae. The light curves thus obtained are in good agreement with the oberved light curves of recurrent novae (Kato 1990a, b; 1991). Taking into account the recent progress of opacity (Rogers & Iglesias 1992; Iglesias & Rogers 1993), we have applied this method to a classical nova, Nova Cygni 1978, and succeeded in reproducing the light curves (Kato 1994).

2.2. *Basic Equations*

We assume steady state and spherical symmetry to calculate structures of mass-losing envelopes. The validity of steady-state approximation will be discussed in detail in § 6.3. Other acceleration mechanisms which may occur outside the photosphere such as line or dust driven winds are not incorporated from the reason that will also be discussed in § 6.2. When the envelope expands to a large size of $\sim 100\ R_\odot$, the companion star is engulfed by the envelope. Then the frictional process between the envelope and the companion star produces heat and it behaves as an energy source like nuclear burning. It may accelerate the wind mass loss. This effect will be separately examined in § 5.

The structure of the mass-losing envelope at any particular stage in the decline phase of nova is described by the following equations. The equation of motion is

$$v\frac{dv}{dr}+\frac{1}{\rho}\frac{dP}{dr}+\frac{GM}{r^2}=0\,, \tag{1}$$

where M is the white dwarf mass, v the velocity, P the total pressure, ρ the density, and r the radius. The total pressure P is the sum of gas and radiation pressures, i.e.,

$$P=\frac{\rho kT}{\mu m_a}+\frac{1}{3}aT^4\,, \tag{2}$$

where T is the temperature, μ the mean molecular weight, k the Boltzmann constant, m_a the atomic mass unit, and a the Steffan-Boltzmann radiation constant.

The continuity equation in spherical steady flows is

$$4\pi r^2\rho v=\text{constant}\equiv\dot{M}\,, \tag{3}$$

where $\dot{M}$ is the wind mass-loss rate. We assume that the radiation energy is transported by the diffusion process from the bottom of the envelope to the photosphere, i.e.,

$$\frac{dT}{dr}=-\frac{3\kappa\rho L_r}{16\pi acT^3r^2}\,, \tag{4}$$

where L_r is the diffusive luminosity at r, κ the opacity, and c the velocity of light. Although the convective condition is sometimes satisfied somewhere in the envelope solutions, we have neglected the convective energy transport because its effect is very small in outflowing matter with supersonic velocities. The effect of convection will be examined in detail in § 6.4. An integrated form of the energy conservation equation is written as

$$L_r+\dot{M}\left(\frac{v^2}{2}+w-\frac{GM}{r}\right)=\text{constant}\equiv\Lambda_{\rm tot}\,, \tag{5}$$

where w is the specific enthalpy, which is given by

$$w=\frac{5}{2}\frac{kT}{\mu m_a}+\frac{4aT^4}{3\rho}\,, \tag{6}$$

The total luminosity $L_{\rm tot}$ measured in a stationary frame is the summation of the diffusive luminosity and the advection luminosity,

$$L_{\rm tot}=L_r+L_{\rm adv}\,, \tag{7}$$

where the advection luminosity is the energy flux of radiation trapped in the gas and moves with it, i.e.,

$$L_{\rm adv}=\frac{4aT^4}{3\rho}\dot{M}\,. \tag{8}$$

The photospheric luminosity is therefore the summation of the diffusive luminosity and the advection luminosity at the photosphere, but usually the advection luminosity is very small, that is, as small as 1% or less and it can be neglected.

These equations are essentially the same as those in previous works (Finzi & Wolf 1971; Żytkow 1972; Ruggles & Bath 1979; Kato 1983b). We have solved these equations from the bottom of the envelope (i.e., the white dwarf surface) to the photosphere.

2.3. *Conditions at the Critical Point*

In order to specify a solution for a particular stage of the decay phase of nova, we need four boundary conditions for four basic differential equations described in the previous subsection. These four boundary conditons are set at the sonic point, the photosphere, and the bottom of the envelope. The first boundary condition is set at the sonic point, because we need a wind solution in which the velocity is very close to zero near the bottom of the envelope but it gradually increases in the envelope and finally exceeds the sound speed far from the white dwarf surface. There exist well known conditions to specify such a solution. Differentiating equation (3) by r and substituting it into equation (1), we have

$$\frac{d\ln v}{d\ln r}=\left[2\frac{kT}{\mu m_a}-\frac{GM}{r}-\frac{d\ln T}{d\ln r}\left(\frac{kT}{\mu m_a}+\frac{4aT^4}{3\rho}\right)\right]\Bigg/\left(v^2-\frac{kT}{\mu m_a}\right). \quad (9)$$

Then the solution must satisfy the following conditions,

$$2\frac{kT}{\mu m_a}-\frac{GM}{r}-\frac{d\ln T}{d\ln r}\left(\frac{kT}{\mu m_a}+\frac{4aT^4}{3\rho}\right)=0\,, \quad (10)$$

and

$$v^2-\frac{kT}{\mu m_a}=0\,, \quad (11)$$

at the same time (Bondi 1952). The position where both conditions (10) and (11) are satisfied at the same time is called *critical point*. This point usually lies in the middle of the acceleration region. When the critical point lies inside the envelope, i.e., between the bottom of the envelope and the photosphere, we consider it as an optically thick wind solution.

The acceleration mechanism of the flow can be understood analogously to the Laval nozzle. After the flow passed the narrowest position of the nozzle, gas is accelerated from subsonic to supersonic according to the increasing cross section of the nozzle. In our spherical wind mass loss, the increase of the cross section corresponds to the increase in the area of spherical shell, i.e., r^2-dependence in equation (3). Therefore, the upper region of the critical point has a spherical structure (Kato 1983a) rather than a plane-parallel structure because the pressure scale height there is the same order of magnitude as the radius r.

2.4. *Surface Boundary Condition and Occurrence of Optically Thick Wind*

The second boundary condition is the photospheric boundary condition. Eddington approximation is widely used in the calculation of stellar evolution. The photosphere in the Eddington approximation is defined as the point where the optical depth τ reaches $\frac{2}{3}$ in the integration from far outside the star. This is valid for a star with a static plane-parallel atmosphere but inappropriate for a mass-losing envelope with a very extended structure. In such a case the density does not drop quickly as in usual cases. Instead it decreases as slow as r^{-2} near the photosphere. This is easily seen from equation (3) assuming a constant velocity.

Here, we adopt the surface boundary conditions proposed by Kato (1983a):

$$L_{\rm ph}=4\pi r_{\rm ph}^2\sigma T_{\rm ph}^4\,. \quad (12)$$

$$\tau_{\rm ph}=\kappa_{\rm ph}\rho_{\rm ph}r_{\rm ph}\sim 2.7\,. \quad (13)$$

The optical depth, $\tau\equiv\kappa\rho r$, is defined by a product of local variables not by an integral from far outside the star. In steady state mass-losing envelopes, the optical depth τ at the photosphere, where the equation (12) is satisfied, is always larger than 8/3 (Kato 1983a; Quinn & Paczyński 1985). Therefore, we practically adopt condition (13) in our calculation. These surface boundary conditions (12) and (13) are the same as those in Paczyński & Prószyński (1986) for mass-loss solutions in X-ray bursts, though they adopt slightly larger values of $\tau_{\rm ph}$ ($3<\tau_{\rm ph}<5$).

These photospheric conditions for extended envelopes were theoretically examined by Kato (1985) in relation to the occurrence of optically thick winds. She assumed several types of the surface boundary conditions with spherical structure and found the condition whether optically thick winds occur or not. More detailed discussions appear in Appendix A.

In what follows we briefly explain the reason why condition (13) is adopted. When the diffusive energy flux, which comes from deep inside the envelope, is much smaller than the Eddington luminosity, a static envelope exists and it has a plane-parallel structure. When the luminosity increases up very close to the Eddington luminosity, the envelope begins to expand. The photospheric radius increases and the structure of the envelope near the surface region changes from plane-parallel to spherical. In other words, the pressure scale height of the envelope becomes as large as the radius of the envelope itself. When the luminosity, L_r, exceeds the maximum value, $L_{\rm max}$, there exists no static solution as shown in Appendix A. Here, $L_{\rm max}$ is defined as

$$L_{\rm max}=L_{\rm Edd}(1-\tfrac{5}{4}\chi)\,, \quad (14)$$

where $L_{\rm Edd}$ is the Eddington luminosity defined by

$$L_{\rm Edd}=\frac{4\pi cGM}{\kappa}\,, \quad (15)$$

and

$$\chi=\frac{2kT_{\rm ph}r_{\rm ph}}{GM\mu m_a}\,. \quad (16)$$

This maximum value is very close to but slightly smaller than the Eddington luminosity, because χ is less than 0.01 for typical nova case. In the solution with the maximum luminosity (14), the optical depth at the photosphere becomes

$$\tau=\kappa_{\rm ph}\rho_{\rm ph}r_{\rm ph}=\tfrac{8}{3}\,. \quad (17)$$

The value of $\frac{8}{3}$ is a characteristic property of the static solution with the maximum luminosity (see Appendix A for more details).

Here we define two special solutions, one for static and the other for wind solution. The first one is the static solution with the maximum luminosity $L_{\rm max}$ defined by equation (14) so that we call it *maximum static solution.* The second one is the wind solution in which the critical (sonic) point is close to the photosphere. We call it *minimum wind solution.* In wind solutions, matter is accelerated inside/near the sonic point. So there cannot exist optically thick wind solutions having the sonic point far outside the photosphere. When and only when condition (13) is applied, the structures of these two special solutions are almost identical with each other, that is, optically thick winds start from the maximum static solution continuously. In other words, we may consider that the occurrence of optically

thick winds can be detected by the condition of $L = L_{max}$ for static solutions and such static solutions are smoothly replaced by wind solutions that has similar structures to the maximum static solutions.

If we assume a larger value of τ at the photosphere, such as 1000 instead of 2.7, for example, the structure of the minimum wind solution deviates largely from that of the maximum static solution. Only when we assume that τ at the photosphere is close to or as small as 8/3, the structure of the minimum wind solution becomes almost identical to the structure of the maximum static solution. These properties indirectly support the acceptance of the boundary conditions (12) and (13). More detailed discussions appear in Appendix A.

The envelope solution at point D in Figure 1 corresponds to the static structure with the maximum luminosity. On the other hand, the structure of the minimum wind solution, in which the critical (sonic) point is close to the photosphere, is almost identical to that of the static solution at point D. We have wind solutions sufficiently close to point D as shown by Kato (1985).

2.5. *Inner Boundary Condition*

The third boundary condition is set at the bottom of the envelope, i.e., at the surface of the white dwarf. In the course of nova decay phase, nova envelope is in the thermal equilibium. Here we mean by the word "thermal equilibrium" that the energy lost from the photosphere is balanced with the energy generated by nuclear burning (e.g., Fig. 1 of Prialnik 1986). We assume that no diffusive energy is coming from inside the white dwarf, i.e.,

$$L_r = L_n \quad \text{at} \quad r = R_{WD} . \tag{18}$$

where the energy flux by nuclear burning is calculated from

$$L_n = \int_{R_{WD}}^{r_{ph}} X\epsilon_H dM_r , \tag{19}$$

and X is the hydrogen mass content, ϵ_H the nuclear energy generation rate of hydrogen per unit mass, M_r the mass within the radius r. We construct a sequence of steady state and static solutions to follow a decay phase of nova. In this sequence, the envelope mass is gradually decreasing with time. Therefore, we need to specify the solution with a given envelope mass, i.e.,

$$\Delta M \equiv \int_{R_{WD}}^{r_{ph}} dM_r = \text{given} . \tag{20}$$

where ΔM is the envelope mass around the white dwarf. This is the last (fourth) boundary condition.

2.6. *Numerical Method*

Originally we have four basic equations, i.e., equation of motion (1), continuity equation (3), energy transfer equation (4), and energy conservation equation (5), each of which is a first order differential equation. Two of these equations can be integrated as seen in equations (3) and (5). Two integral constants, $\dot{M}$ and Λ_{tot}, are determined as eigenvalues of the boundary-value problem when we specify four boundary conditions, i.e., equations (10) and (11) at the critical point, equation (12) at the photosphere (13), equation (18) at the bottom of the envelope, and equation (20). Thus, one unique solution is specified for a given envelope mass of nova. Therefore, we obtain one solution corresponding to one point in the course of nova decay phase, i.e., from point C to point D in the theoretical H-R diagram (Fig. 1).

The fact that the mass loss rate is an eigenvalue of the boundary-value problem means that the value itself is determined with high numerical accuracy. One of the advantages of the optically thick wind theory lies in the accurate determinations of the mass-loss rate, the photospheric temperature, the luminosity, and so on. This accurate determination is essential to construct reliable light curves. On the contrary, time-dependent calculations often encounter numerical difficulties near the surface region when the envelope expands considerably. These numerical difficulties prevent from reproducing the light curves.

Equations (1) and (4) are integrated numerically by using a trapezoidal implicit method (Appendix B for more details). We first assume trial values of temperature T_{cr} and position r_{cr} at the critical point. We integrate outwards with a trial value of the density ρ_{cr} and get a value of τ at a point where equation (12) is satisfied. If τ is not sufficiently close to 2.7 ($\sim$8/3), we repeat the integration with different ρ_{cr} until we reach the final value which satisfies both equations (12) and (13).

After that, we integrate inward from the sonic point to the surface of the white dwarf, $r = R_{WD}$, and find an appropriate value of T_{cr} which satisfies inner boundary condition (18). Finally, we find an appropriate value of r_{cr} which satisfies condition (20). We need several to ten iterations for each step of iterations so that typically about four to five hundred iterations in total (for example, $10 \times 7 \times 7 = 490$) are needed to satisfy a given accuracy of 0.1%.

We have constructed sequences for the white dwarf masses of 1.33, 1.2, 1.1, 1.0, 0.9, 0.8, 0.7, 0.6, 0.5, and 0.4 $M_\odot$. The Chandrasekhar radius is assumed for white dwarfs less massive than 1.3 $M_\odot$. For more massive ones, a value calculated by Nomoto, Thielemann, & Yokoi (1984) is assumed, i.e. $\log (R_{WD}/R_\odot) = -2.417$ for 1.33 $M_\odot$ white dwarfs.

The chemical composition of the envelope is assumed to be uniform with $X = 0.35$, $Y = 0.33$, C = 0.1, O = 0.2, and $Z = 0.02$ for hydrogen, helium, carbon, oxygen, and heavy elements, respectively, for classical novae. For comparison, we also examine the solar composition case of $X = 0.7$, $Y = 0.28$, and $Z = 0.02$ in § 4. Other chemical compositions such as neon-rich or CO-rich are discussed in § 6.1. We used the OPAL opacity tables (Rogers & Iglesias 1992; Iglesias & Rogers 1993) with Fe intermediate coupling, in which the density extends to $\log R \geq -7.0$, where $R \equiv \rho(\text{g cm}^{-3})/(T/10^6 \text{ K})^3$. A quadratic interpolation formula has been used to get a value between two grid points of the opacity table. The deviation of the interpolated value from the true value is expected to be as small as a few percent (Rogers & Iglesias 1992). To obtain the mean molecular weight of electron, we solved Saha's equations of ionization equilibrium among various ionization stages of hydrogen, helium, carbon, oxygen, and neon.

3. WIND SOLUTIONS OF NOVAE

Specifying the white dwarf mass and the envelope mass, we obtain a steady state wind solution. First, we describe the basic characteristics of each wind solution. Next, we construct a sequence consisting of steady state solutions and static solutions by decreasing the envelope mass gradually. Finally, several light curves are made based on the sequences thus obtained. These theoretical light curves should be compared with observed ones to draw various physical parameters on novae, e.g., the white dwarf mass, the envelope mass, the chemical composition, the distance to the nova, and so on.

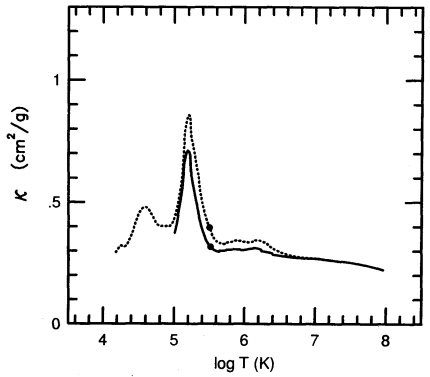

FIG. 2.—Run of the opacity against the temperature for two wind solutions on 1.0 $M_\odot$ white dwarf with the critical point of $r_{cr} = 0.65\ R_\odot$ (*dotted curve*) and $r_{cr} = 0.2\ R_\odot$ (*thick curve*). The strong peak due to iron lines is prominent around log T(K) = 5.2. The small peak around log T(K) = 4.58 is due to ionizations of carbon and oxygen. We have assumed the chemical composition of the envelope to be $X = 0.33$, $Y = 0.35$, C = 0.1, O = 0.2, and $Z = 0.02$.

3.1. *Wind Solutions*

Two typical wind solutions on a 1.0 $M_\odot$ white dwarf are shown in Figures 2–4 to explain the basic characteristics of steady state wind solutions. Dotted lines correspond to the solution in which the critical point lies at $r_{cr} = 0.65\ R_\odot$. Solid lines denote the case of the critical point at $r_{cr} = 0.2\ R_\odot$. The photospheric temperatures of these solutions are log T_{ph}(K) = 4.182 and 5.007, the photospheric radii are $r_{ph} = 24.5\ R_\odot$ and $0.643\ R_\odot$, the envelope masses are 9.46×10^{-6} and $2.86 \times 10^{-6}\ M_\odot$, the wind mass-loss rates are 1.14×10^{-4} and $5.29 \times 10^{-6}\ M_\odot\ \mathrm{yr}^{-1}$, the velocities of matter at the photosphere are 361 and 817 km s^{-1}, respectively.

Figure 2 shows the opacity distribution of these two solutions against the temperature. The sharp peak around log $T = 5.20$ is due to the effect of iron lines and the small peak around log $T = 4.58$ corresponds to ionization zones of carbon and oxygen. Such a large enhancement in the opacity is the origin of strong acceleration of winds. The Eddington luminosity and the diffusive luminosity of the solution are shown in Figure 3. The Eddington luminosity sharply decreases and reaches the minimum at log r(cm) = 10.92 and log r(cm) = 10.42, respectively. These positions correspond to the opacity peaks due to iron lines. This strong decrease in the

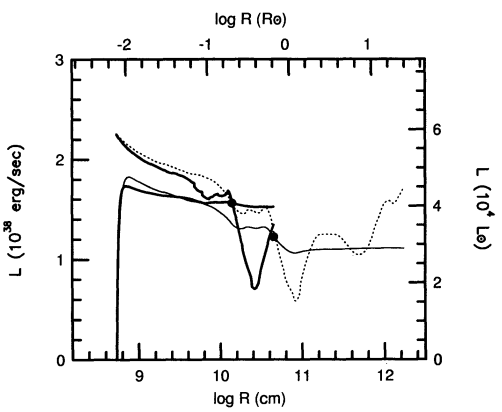

FIG. 3.—Diffusive luminosity is plotted together with the Eddington luminosity for the same solutions as in Fig. 2. There is a strong super-Eddington region around log R(cm) = 10.92 and 10.42, each of which corresponds to the opacity peak due to iron lines. The filled circle denotes the critical point.

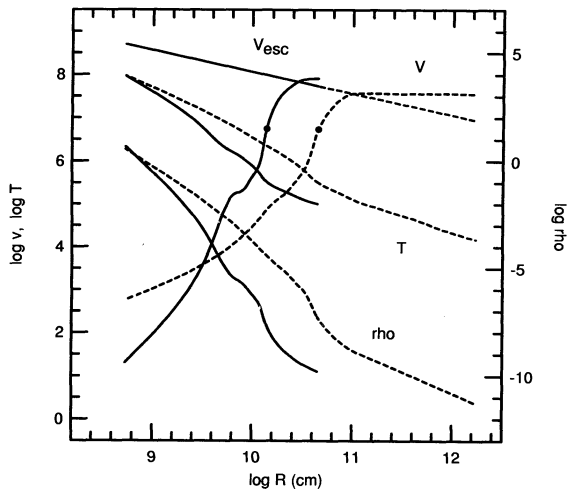

FIG. 4.—Density, the temperature, the velocity, and the escape velocity are plotted against the radius. The thick and dotted curves denote the models with $r_{cr} = 0.2\ R_\odot$ and $r_{cr} = 0.65\ M_\odot$, respectively.

Eddington luminosity blocks the diffusive luminosity and causes strong acceleration of matter. Figure 4 clearly shows that the velocity increases steeply around the critical point where the Eddington luminosity drops. At the same time, the density goes down quickly and the diffusive luminosity also decreases as shown in Figures 3 and 4. A part of the diffusive energy flux is consumed to push envelope matter up against the gravity near the critical point.

Then, we have obtained so many wind solutions (about 500 in total) for various envelope and white dwarf masses. In what follows, we briefly summarize the basic characteristics of wind solutions. The position of a wind solution in the H-R diagram is shown in Figure 5 for various envelope and white dwarf masses. The dashed line corresponds to wind solutions while the solid line denotes static (no wind) solutions. No optically thick winds occur on a 0.4 $M_\odot$ white dwarf. Figure 6 shows the mass decreasing rate of the envelope against the envelope mass, where the decreasing rate is the summation of the wind mass-loss and the mass decreasing rate due to hydrogen

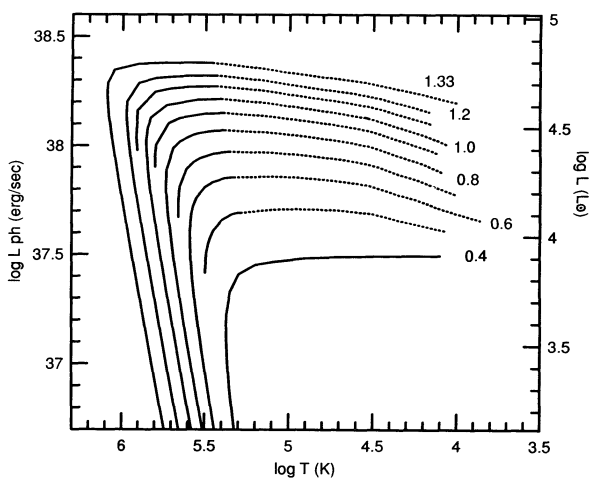

FIG. 5.—Evolutionary tracks of the decay phase of novae are plotted in the theoretical H-R diagram. Each curve corresponds to different white dwarf mass, i.e., 1.33, 1.2, 1.1, 1.0, 0.9, 0.8, 0.7, 0.6, 0.5, and 0.4 $M_\odot$. The mass of white dwarf is attached to each curve. Dashed part of the curve denotes the wind phase.

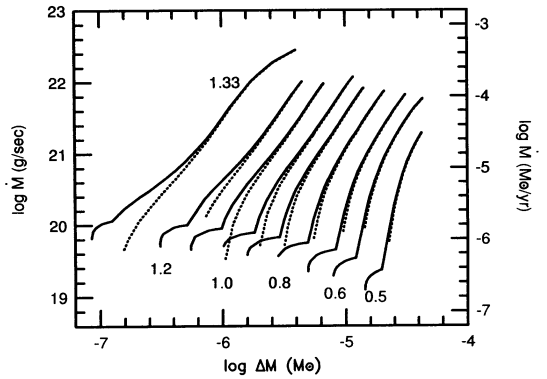

FIG. 6.—Mass decreasing rate of the envelope (*solid lines*), the summation of the wind mass-loss rate and the mass decreasing rate due to hydrogen burning, is plotted against the envelope mass. The mass of the white dwarf is attached to each curve. The dashed one denotes the wind mass-loss rate.

burning, i.e.,

$$\dot{M}_{\rm env} = \dot{M} + \dot{M}_{\rm nuc} , \tag{21}$$

where the mass decreasing rate due to nuclear burning is estimated by

$$\dot{M}_{\rm nuc} = \frac{L_n}{X\epsilon_{\rm H}} . \tag{22}$$

As the envelope mass is decreasing, the wind mass-loss rate is also decreasing. When the envelope mass reaches some critical value, the wind stops. The folded portions of each curve in Figure 6 correspond to point D in Figure 1, i.e., the critical static solution with maximum luminosity. After that point, the envelope mass is further decreasing but due only to hydrogen burning.

The mass-loss rate is gradually decreasing with the envelope mass being decreased as shown in Figure 6. On the other hand, the photospheric temperature is increasing as shown in Figure 7. The photospheric luminosity is also increasing a little bit as shown in Figure 5. This is because a part of the diffusive energy flux is consumed to drive the wind mass loss, mainly to push the matter up againt the gravity. The lower the surface temperature, the larger the mass-loss rate, i.e., as large as $10^{-4}\,M_\odot$ yr^{-1}. Therefore, the diffusive luminosity is much more consumed for solutions with lower surface temperatures. The wind mass-loss rate becomes as small as $10^{-6}\,M_\odot$ yr^{-1} or less just before it stops near point D.

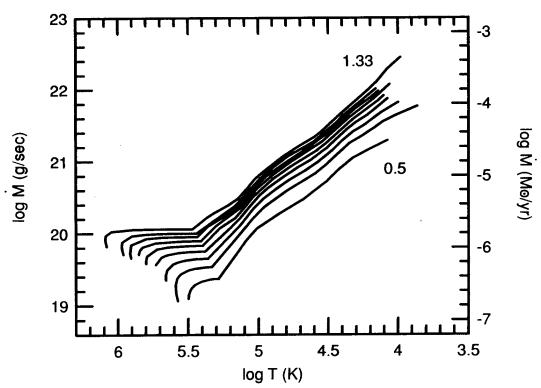

FIG. 7.—Mass decreasing rate of the envelope is plotted against the photospheric temperature.

It is remarkable that the slopes in Figure 7 are almost the same among various white dwarf masses at least for the region of log $T_{\rm ph}$(K) = 4–5. Therefore, we are able to make a simple empirical formula of mass-loss rate:

$$\log \dot{M}\ ({\rm g\ s^{-1}}) = -1.49 \log (T_{\rm ph}/10^5\ {\rm K}) + b , \tag{23}$$

where b depends on the white dwarf mass and is tabulated in Table 1. The maximum errors of these empirical formulae are smaller than 0.04.

3.2. *Sequence of Wind Solutions*

Constructing a sequence consisting of steady wind and static solutions described in the previous subsection, we can follow the evolution of decay phase of novae (Kato 1983b, 1990a, b, 1991; Kato & Hachisu 1988, 1989). If the white dwarf mass is given, one particular solution on the sequence is specified by the envelope mass. The envelope mass is large at early phase and then gradually decreases in time due both to wind mass loss and to hydrogen burning. Then the star moves blueward in the H-R diagram. When the envelope mass decreases to some critical value, the wind stops. This point corresponds to point D in Figure 1. After the wind stops, the envelope mass is decreased only by hydrogen shell burning until point E in Figure 1. After point E, hydrogen shell burning vanishes, the envelope cools down to point A.

We introduce an evolutionary timescale in our steady state sequences by calculating time interval between two wind solutions as follows:

$$\Delta t = \int_{M_2}^{M_1} \frac{dM}{\dot{M}_{\rm env}} , \tag{24}$$

where the subscripts 1 and 2 denote two wind solutions with envelope mass M_1 and M_2, respectively. Therefore, the total duration of the wind phase (from point C to point D in Fig. 1) is calculated as

$$t_{\rm wind} = \int_{M_{\rm D}}^{M_{\rm C}} \frac{dM}{\dot{M}_{\rm env}} , \tag{25}$$

where $M_{\rm C}$ and $M_{\rm D}$ are the envelope mass at points C and D, respectively. After the wind mass loss stops at point D, the

TABLE 1

EMPIRICAL RELATION OF MASS-LOSS RATE VERSUS PHOTOSPHERIC TEMPERATURE[a]

$M_{\rm WD}$ ($M_\odot$)	b
1.33	20.78
1.2	20.72
1.1	20.67
1.0	20.62
0.9	20.55
0.8	20.49
0.7	20.38
0.6	20.24
0.5	20.01

[a] Mass-loss rate is given by equation (23). We assume the chemical composition of the envelope to be $X = 0.33$, $Y = 0.35$, C = 0.1, O = 0.2, and $Z = 0.02$ and use the corresponding OPAL opacity.

TABLE 2

TIMESCALES OF DECAY PHASE OF CLASSICAL NOVAE[a]

M_{WD} ($M_\odot$)	t_{wind} (yr)	t_{static} (yr)
1.33	0.11	0.038
1.2	0.26	0.15
1.1	0.39	0.34
1.0	0.61	0.74
0.9	0.87	1.40
0.8	1.4	2.7
0.7	2.4	5.3
0.6	4.0	8.9
0.5	7.4	16.8
0.4	...	61

[a] We assume the chemical composition of the envelope to be $X = 0.33$, $Y = 0.35$, C = 0.1, O = 0.2, and $Z = 0.02$ and use the corresponding OPAL opacity

envelope mass decreases only by nuclear burning. The duration of static phase is also calculated by

$$t_{static} = \int_{M_E}^{M_D} \frac{dM}{\dot{M}_{env}}, \quad (26)$$

Thus, we have calculated evolutional time of our sequences in Table 2 (see also Kato & Hachisu 1988, 1989).

3.3. *Theoretical Light Curves*

Now we are able to obtain theoretical light curves of novae as shown in Figure 8. Light curves are plotted for the white dwarf masses of 1.33, 1.2, 1.1, 1.0, 0.9, 0.8, 0.7, 0.6, and 0.5 $M_\odot$. It should be noted that we cannot reproduce the rising phase of novae or around the luminosity peak because the steady state assumption is not valid there.

More massive white dwarfs show more rapid development in their light curves. It is because the envelope mass is much smaller on more massive white dwarfs than on less massive ones as shown in Figure 6, whereas the wind mass-loss rate is almost the same for the same photospheric temperature as shown in Figure 7, i.e., its weak dependence on the white dwarf mass.

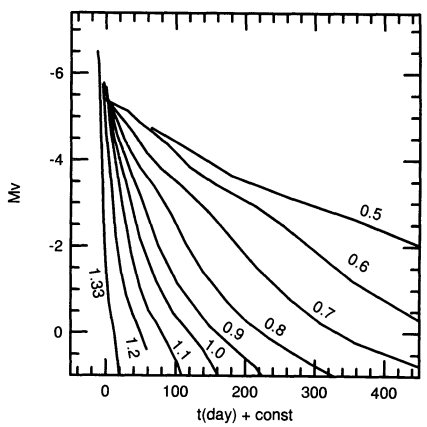

FIG. 8.—Theoretical light curves of classical novae are plotted for various white dwarf masses. The zero point of the abscissa should be determined from the initial envelope mass.

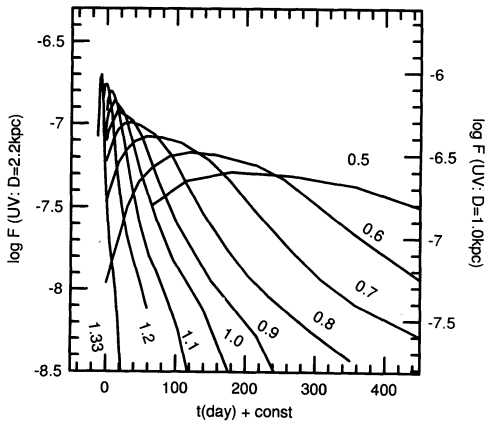

FIG. 9.—Theoretical UV light curves for the same sequence as in Fig. 8

Figure 9 shows ultraviolet (UV) light curves for the same sequences as in Figure 8. The flux of UV, F(UV), covers the region of wavelength 911 Å–3250 Å and measured in units of ergs cm^{-2}. The distance to the star is assumed to be 2.2 kpc in the left side ordinate but 1.0 kpc in the right side ordinate. The peak of UV light curves is always reached after the peak of the corresponding visual light curves. This is because the wavelength at the spectral maximum enters UV region after it passes through the visual band with the constant bolometric luminosity.

The wind mass-loss rate, $\dot{M}$, is also plotted in Figure 10 against time for the same sequences as in Figure 8. The photospheric temperature, the photospheric radius, and the velocity of matter at the photosphere are also shown in Figures 11, 12, and 13, for the same sequences as in Figure 8.

3.4. *Light Curve Analysis of Classical Nova, Nova Cygni 1978*

Now our theoretical light curves should be compared with the observational data to see whether or not our wind theory is applicable to real nova phenomena. Nova Cygni 1978, a moderately fast nova, is a good candidate in the sense that it has been well observed in many wavelengths. The data in two wavelengths of visual and UV are fitted to our theoretical visual and UV light curves as shown in Figure 14. The optical data observed by Gallagher et al. (1980) are plotted in Figure 14*a* by open circles. It should be noted that these are *y*-band magnitude. The *y*-band is a rather narrow band compared with the *V*-band and supposed to be almost line-free, that is, it

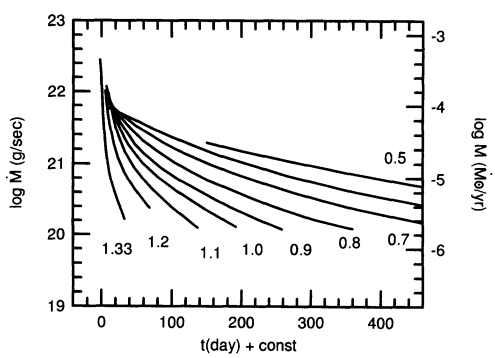

FIG. 10.—Wind mass-loss rate is plotted against time for the same sequences as in Fig. 8.

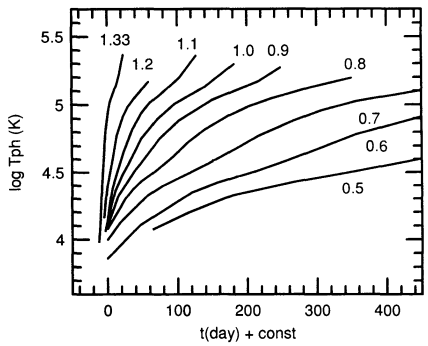

FIG. 11.—Change of the photospheric temperature in time for the same sequences as in Fig. 8.

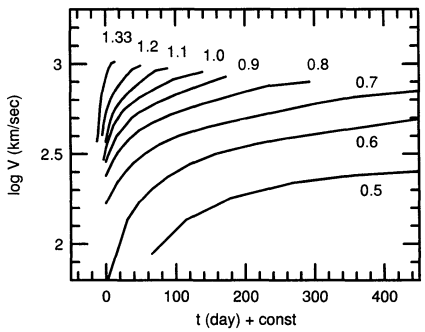

FIG. 13.—Velocity of matter at the photosphere is plotted against time for the same sequences as in Fig. 8. It is gradually increasing up to ~ 1000 km s^{-1} during the decay phase of novae.

is a good tracer of the continuum. On the other hand, the V-band is contaminated by line emissions in the nebula phase of novae and does not represent the continuum.

In this sense, the y-band magnitude is suitable to our fitting of light curves, because our theoretical light curves does not include line emissions/absorptions but trace only the continuum radiation. The y-magnitude does follow the V-band magnitude at the relatively early phase of novae but gradually deviates in the later phase of novae (Duerbeck, Rindermann, & Seitter 1980; Kaler 1986), where emission lines dominate (after $m_V \geq 10$). If the radiation has no line emissions/absorptions, y-magnitude is very close to V-magnitude. Therefore, our theoretical y-magnitude is almost equal to our theoretical V-magnitude.

Figure 14*b* shows a light curve in UV observed by the *IUE* satellite (Stickland et al. 1981). Open circles denote the UV flux (1140–3290 Å). The infrared (IR) flux becomes large and comparable to the UV flux (Stickland et al. 1981) in the late phase of the outburst. It is most likely that the IR emission is dust-origin in the circumstellar and that this IR flux comes from the UV radiation which is emitted at the photosphere. Therefore, the original UV flux is equal to the sum of UV and IR fluxes observed. Such an estimated original UV flux is denoted by filled circles in Figure 14*b*.

Our theoretical light curves, which are the same models as in Figures 5–13, are also plotted in Figure 14. In this figure, we move our theoretical light curves in the vertical direction to fix the distance to the star or in the horizontal direction to fix the origin of time. First, we will fit our UV light curves to the observed UV data: it has a peak at about $t = 785$ days (i.e., 23 days after the optical maximum). The peaks of five theoretical UV light curves are fixed at $t = 785$ days then we easily find

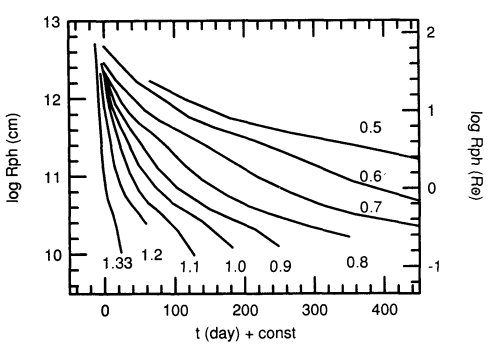

FIG. 12.—Change of the photospheric radius in time for the same sequences as in Fig. 8.

that among five theoretical UV light curves, the 1.0 $M_\odot$ model is the best fit one around/near the peak. The 0.9 $M_\odot$ model still seems to be consistent with the data, but the 1.1 $M_\odot$ model is too steep. The other two light curves of the 1.2 and 1.3 $M_\odot$ models are also too steep and may be excluded. So we adopt the model of 1.0 $M_\odot$ as the best-fit model and obtained the distance of 2.87 kpc.

Next, we seek the best fit one for the optical light curve. Since we have already fixed the origin of time by the UV peak, we can move the light curves in the vertical direction and get the distance to the star which is independent of the distance determination by the UV light curves. We easily see that the 1.0 $M_\odot$ model is the best fit one. The models of 0.9 and 1.1 $M_\odot$ seem not to be consistent with the observational data. The other models of 1.2 and 1.33 $M_\odot$ are too steep and may be excluded. The distance to the star is independently obtained by the fitting of the 1.0 $M_\odot$ model to be 3.21 kpc with the

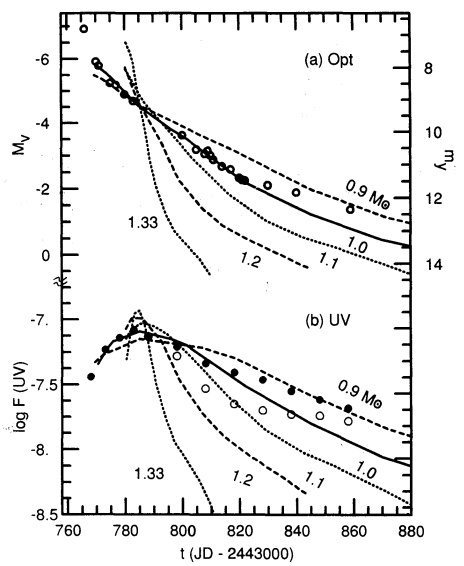

FIG. 14.—Theoretical and observational light curves for the decay phase of classical novae. Theoretical ones are denoted by lines. White dwarf mass is attached to each curve. (*a*) Optical light curves. The left ordinate shows the absolute visual magnitude for the theoretical curves. Observational data of Nova Cygni 1978 (Gallagher et al. 1980) are shown by open circles. Its apparent y-magnitude is written on the right ordinate. (*b*) UV light curves. Open circles denote the UV flux (1140–3290 Å) and filled circles do the summation of the UV and IR fluxes (>12000 Å) in the units of ergs cm^{-2} s^{-1} (Stickland et al. 1981). Theoretical UV flux, $F = L_{UV}/4\pi D^2$, is also shown by lines, where D is the distance to the star and assumed to be 2.88 kpc.

reddening of $A_V = 1.2$ (Stickland et al. 1981) or 3.06 kpc with $A_V = 1.3$ (Gallagher et al. 1980). This is in a reasonable agreement with the 2.87 kpc distance obtained from the UV light curve fittings.

The distances thus obtained seem to be consistent with the other determinations of distance, for example, ~1.0–3.3 kpc by Duerbeck et al. (1980). Another estimate of the distance may come from the UV flux. If the star emits only UV radiation at the Eddington luminosity, the distance is calculated to be $D = 3.6$ kpc by equating the flux, $F = L_{\rm Edd}/4\pi D^2$, equal to the observed peak flux, $\log F = -7$, where the opacity is assumed to be 0.316 from the model at the peak of the UV light curve. This is an upper limit to the distance.

The expansion velocity in Nova Cygni 1978 has been estimated as $v = 760$ km s^{-1}, i.e., $\log v(\mathrm{km\ s^{-1}}) = 2.88$ at 56 days after the optical maximum from an *IUE* high-dispersion spectrum (Stickland et al. 1981). The corresponding time in Figure 13 is $t = 44$ days. As our theoretical curve for 1.0 $M_\odot$ gives $\log v(\mathrm{km\ s^{-1}}) = 2.80$ at that time. Thus, the observational velocity is also in good agreement with our theoretical value for the 1.0 $M_\odot$ white dwarf model.

In summary, two independent light curve fittings of Nova Cygni 1978 consistently indicate that the white dwarf mass is about 1.0 $M_\odot$ and the distance to the nova is between 2.9 and 3.2 kpc. These results also support the validity of our optically thick wind theory, at least, for the decay phase of novae.

4. EFFECT OF OPAL OPACITY

The advent of the OPAL opacity enables us to reproduce reasonable light curves. In the present section, we show the reason why the OPAL opacity makes good quality light curves compared with the old opacity. Figure 15 shows the run of the opacity for wind solutions on a 1.0 $M_\odot$ white dwarf; one for the OPAL opacity (*solid line*) and the other for the old opacity (*dashed line*). The solid curve denotes the model with the OPAL opacity for the chemical composition of $X = 0.70$ and $Z = 0.02$. This solution has the critical point at $\log r_{\rm cr}$ (cm) = 10.843, the surface temperature $\log T_{\rm ph} = 3.846$, the wind mass-loss rate $\dot{M} = 2.28 \times 10^{-4}\ M_\odot\ \mathrm{yr}^{-1}$, the envelope mass $\Delta M = 2.72 \times 10^{-5}\ M_\odot$. The dashed curve denotes the model with the old capacity for the chemical composition of $X = 0.73$ and $Z = 0.02$, which is taken from Kato (1983b). For the old opacity we used the interpolation formulae proposed by Iben (1975) for $\log T > 6.0$ and by Stellingwerf (1975) for $\log T \lesssim 6.0$. These formulae are based on Los Alamos opacities (Cox & Stewart 1970a, b; Cox, King, & Tabor 1973). This solution has the critical point at $\log r_{\rm cr}$ (cm) = 12.500, the surface temperature $\log T_{\rm ph} = 3.824$, the wind mass loss rate $\dot{M} = 1.42 \times 10^{-4}\ M_\odot\ \mathrm{yr}^{-1}$, the envelope mass $\Delta M = 5.61 \times 10^{-5}\ M_\odot$. The prominent peak due to iron lines appears near $\log T(\mathrm{K}) \sim 5.2$ in the OPAL opacity whereas the largest peak of the old opacity lies at $\log T(\mathrm{K}) \sim 4.0$ due to the hydrogen recombination lines.

It is easily understood that the new opacity may resolve difficulties in the nova wind theory that either the timescale of nova or the wind velocity cannot be successfully reproduced with the old opacity. As shown in § 2.4 optically thick winds occur only when the diffusive luminosity exceeds the minimum value of the Eddington luminosity. With the old opacity, there is a small opacity peak near $\log T(\mathrm{K}) \lesssim 4.0$, which is due to ionization of hydrogen. Then the matter is accelerated just inside this region where the opacity quickly increases outward. The critical point lies in this region, as shown in Figure 15, because it is always located in the region of acceleration. With the OPAL opacity, matter is accelerated at the largest peak of $\log T(\mathrm{K}) \sim 5.2$, which lies deep in the envelope where the density is very high. This is the reason why the mass-loss rate is so large for the case of the OPAL opacity compared with the old solutions.

Figure 16 shows the evolutionary tracks in the H-R diagram for various white dwarf masses with the OPAL opacity for the chemical composition of $X = 0.70$, $Y = 0.28$, and $Z = 0.02$. A part of the 0.6 $M_\odot$ sequence cannot be obtained due to numerical difficulties in which the density is increasing outward near surface region. It is easily seen that point D for various white dwarf masses, where the wind mass loss stops, lies at the same photospheric temperature of $\log T(\mathrm{K}) \sim 5.3$. This is because the main acceleration region lies at $\log T(\mathrm{K}) \sim 5.2$ in both the cases of C/O enhanced and hydrogen-rich materials. The wind mass loss stops after the surface temperature increases higher than that of this strong peak because no prominent peak exists

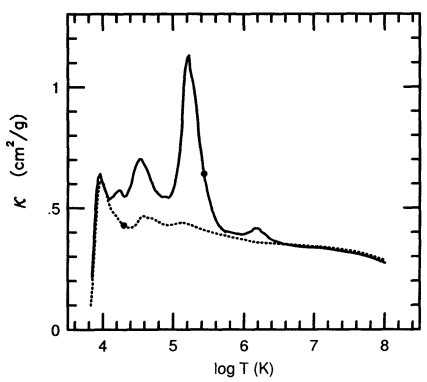

FIG. 15.—Run of the opacity against the temperature for two envelope solutions on the 1.0 $M_\odot$ white dwarf. The thick curve denotes a model with the OPAL opacity of $X = 0.70$, $Y = 0.28$, and $Z = 0.02$, and the dotted curve denotes the old opacity of $X = 0.73$, $Y = 0.25$, and $Z = 0.02$. Peaks are due to iron lines [$\log T(\mathrm{K}) \sim 5.2$], carbon and oxygen [$\log T(\mathrm{K}) \sim 4.5$] and hydrogen [$\log T(\mathrm{K}) \sim 4$] recombination lines. The position of the critical point is denoted by filled circles.

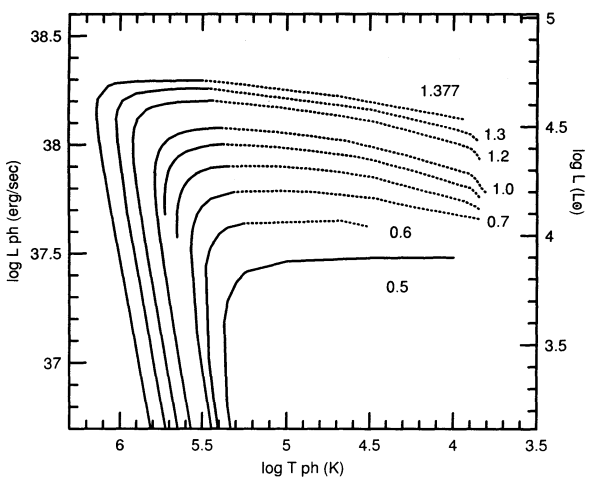

FIG. 16.—Theoretical H-R diagram for the decay phase of novae are plotted. The OPAL opacity for the chemical composition of $X = 0.70$, $Y = 0.28$, and $Z = 0.02$ is used. The white dwarf mass is attached to each curve. A part of the 0.6 $M_\odot$ sequence has not been calculated because of numerical difficulties. Dashed parts of the curves denote the wind phase, while solid parts correspond to the static phase. No optically thick wind occurs for a 0.5 $M_\odot$ white dwarf.

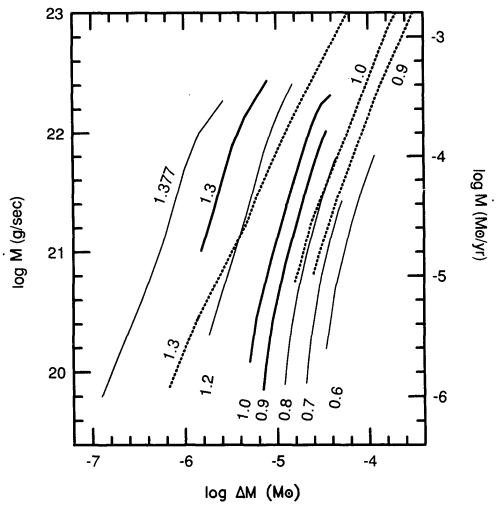

FIG. 17.—Wind mass-loss rate is plotted against the envelope mass. Solid lines denote the wind mass-loss rate with the OPAL opacity, while dotted lines represent those with the old opacity, which are taken from Kato & Hachisu (1988, 1989).

above that. In the old opacity cases, point D is located at much lower temperature. For example, point D lies at $\log T(\mathrm{K}) = 4.74$ for 1.3 $M_\odot$, $\log T(\mathrm{K}) = 4.03$ for 1.0 $M_\odot$, $\log T(\mathrm{K}) = 3.99$ for 0.9 $M_\odot$ white dwarfs (Kato & Hachisu 1988, 1989). This is because the main opacity peak is reached at the helium recombination zone for massive white dwarfs or at the hydrogen recombination zone in less massive white dwarfs, both of which lie at lower temperature region.

Figure 17 shows the comparison of the wind mass-loss rate of nova solutions. Here solid curves denote the value with the OPAL opacity and dotted with the old opacity. The slope of the wind mass-loss rate is similar between them, but the positions of the OPAL ones are systematically shifted leftward compared with the old ones. For the same envelope mass, the mass-loss rate is about several to 10 times larger with the OPAL opacity than that with the old ones. Much higher mass-loss rates for the same envelope mass result in much shorter timescales of nova outbursts.

The timescale of nova duration is summarized in Tables 2–4, where the durations of the wind and static phases are calculated by equations (25) and (26), respectively. The wind phase is defined as from point C to point D, but point C may depend on the initial envelope mass at the ignition. Here, we regard point C as the solution having the lowest temperature in Figure 16. It should be noted that the duration is hardly affected by the exact position of point C, because the mass-loss rate near point C is so large that the star quickly moves leftward. The durations thus obtained are very short compared with the results in our previous papers with the old opacity (Kato & Hachisu 1988, 1989). For example, the durations of the wind and the static phases in the previous results are (1.1 yr, 0.28 yr) for 1.3 $M_\odot$ white dwarf (3.2 yr, 14 yr) for 1.0 $M_\odot$ white dwarf (5.2 yr, 29 yr) for 0.9 $M_\odot$ white dwarf, respectively. On a 0.7 $M_\odot$ white dwarf, no wind occurs, instead the static phase lasts 150 yr as shown in Table 4. With the new opacity, no steady wind occurs on a 0.5 $M_\odot$ white dwarf, but the timescale itself is much shortened (see Table 3). This is because the envelope mass is much reduced by the large enhancement of the new opacity.

With the old opacity, we have failed to reproduce nova light curves. There are two main reasons: one is a long duration time of the wind phase and the other is the low surface temperature of point D. The long duration time forced us to conclude that very massive white dwarfs such as ~ 1.3 $M_\odot$ are needed to obtain rapid evolution of novae. The low temperature of point D causes a sudden change at $t \sim 400$ day in the light curves as seen in Figure 18, because the evolutionary speed is much different between the wind and the static phases.

TABLE 3

TIMESCALES OF DECAY PHASE FOR SOLAR COMPOSITION[a]

M_{WD} ($M_\odot$)	t_{wind} (yr)	t_{static} (yr)
1.377	0.14	0.028
1.3	0.41	0.22
1.2	0.85	0.90
1.0	2.3	4.5
0.7	12.	33.
0.6	24.	55.
0.5	...	270

[a] We assume the chemical composition of the envelope to be $X = 0.70$, $Y = 0.28$, and $Z = 0.02$ and use the corresponding OPAL opacity.

TABLE 4

TIMESCALES OF DECAY PHASE FOR THE OLD OPACITY[a]

M_{WD} ($M_\odot$)	t_{wind} (yr)	t_{static} (yr)
1.3	1.1	0.28
1.2	2.0	2.1
1.0	3.2	14
0.9	5.2	29
0.7	...	150
0.6	...	330
0.4	...	3300

[a] Taken from Kato & Hachisu 1988, 1989, 1991b with chemical composition of $X = 0.73$, $Y = 0.25$, and $Z = 0.02$. Here, point C is defined by $r_{ph} = 10$ $R_\odot$.

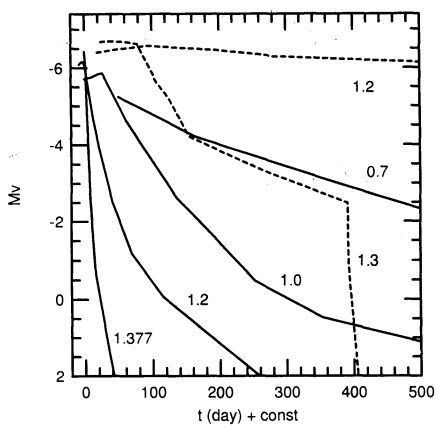

FIG. 18.—Comparison of light curves between the OPAL and the old opacities. Solid curves denote the light curves with the OPAL opacity. Dashed ones represent those with the old opacity. The white dwarf masses are attached to each curve. It is easily seen that the new opacity drastically improves the quality of light curves.

With the OPAL opacity, the large peak at the high-temperature region drastically improves the light curves. The rapid evolution of mass-loss phase smoothly switches to the static phase at point D. This is the reason why we have a smooth light curve during the decay phase of nova through point C to E. Moreover, point D shifts into much higher temperature region so that the connection from the wind to the static phase moves below $M_V > 2$ in the figure, where little interests arise to fit with the observations.

5. EFFECT OF DRAG LUMINOSITY

In this section we examine the effects of drag luminosity during the common envelope phase. As shown in § 3 nova envelope expands greatly and, as a result, the companion star is engulfed by the envelope. Frictional processes between the gaseous matter and the companion star produces thermal energy because the companion star moves in the envelope with supersonic velocity. Although it is unlikely, as mentioned in § 1, that the drag luminosity strongly accelerates mass loss and shortens the nova duration, it is necessary to examine, under the use of the OPAL opacity, whether or not mass ejection is greatly accelerated during the common envelope phase.

We treat the drag luminosity in the same way as our previous paper (Kato & Hachisu 1991a, b): the companion star is assumed to be a zero age main-sequence star just filling its inner critical Roche lobe. Its orbit is also assumed to be circular. We use Patterson's (1983) mass-radius relation for zero age main-sequence stars and Eggleton's (1983) expression for the effective radius of the inner critical Roche lobe. Then the orbit is automatically determined if we specify the masses of the white dwarf and the companion star. For example, the radius of the orbit is 6.6×10^{10} cm for a white dwarf mass $M_{\rm WD} = 1.0\ M_\odot$ and a companion mass $M_{\rm comp} = 0.2\ M_\odot$ as shown in Table 5.

The most important assumption in our treatment is that our calculation is based on one-dimensional (spherical) approximation. The drag luminosity in the common envelope phase is estimated as follows: when the companion star is moving supersonically in the envelope, the drag luminosity generated in the region between r and $r + dr$ can be approximated as

$$dL_{\rm drag} = \rho\,|\,\boldsymbol{v}_{\rm rot} - \boldsymbol{v}_e\,|^3\,dS\,, \tag{27}$$

where ρ is the density of the envelope, $\boldsymbol{v}_{\rm rot} - \boldsymbol{v}_e$ is the relative velocity between the envelope and the companion star, dS is the cross-sectional area of the circular strip between r and $r + dr$ and the circle with a radius R_a, the center of which is located at $r = r_{\rm orb}$. Here the modified accretion radius, R_a, is defined as

$$R_a = \frac{R_0}{1 + (R_0/2H)^2}\,, \tag{28}$$

where H is the local density scale height, and R_0 is the generalized Bondi (1952) radius defined by

$$R_0 = \frac{2GM_{\rm comp}}{(\boldsymbol{v}_{\rm rot} - \boldsymbol{v}_e)^2 + C_s^2}\,, \tag{29}$$

where C_s is the sound velocity at the companion orbit $r_{\rm orb}$ (e.g., Shima et al. 1985; Livio et al. 1990). When the accretion radius, R_a, is smaller than the radius of the companion star, $R_{\rm comp}$, we take the real radius of the companion as R_a in equation (27) instead of equation (28).

Then the total drag luminosity is calculated from

$$L_{\rm drag} = \int \rho\,|\,\boldsymbol{v}_{\rm rot} - \boldsymbol{v}_e\,|^3\,dS\,. \tag{30}$$

If both the density ρ and R_a are constant in space, the drag luminosity (30) becomes the standard expression, i.e.,

$$L_{\rm drag} = \pi R_a^2 \rho\,|\,\boldsymbol{v}_{\rm rot} - \boldsymbol{v}_e\,|^3\,, \tag{31}$$

(e.g., Bodenheimer & Taam 1984; Livio & Soker 1988; Taam & Bodenheimer 1989; Livio et al. 1990). In our one-dimensional calculation the drag luminosity, $dL_{\rm drag}$, is redistributed over the entire spherical shell between r and $r + dr$.

We assume that the envelope has no rotational velocity but a large expansion velocity due to wind, i.e.,

$$\boldsymbol{v}_e = (v_{\rm wind},\, 0)\,, \tag{32}$$

where the first component denotes the radial component and the second one the azimuthal component in the orbital plane, and the rotational velocity of the companion star is given by

$$\boldsymbol{v}_{\rm rot} = (0,\, v_{\rm orb})\,, \tag{33}$$

where

$$v_{\rm orb} = \left[\frac{G(M_{\rm WD} + M_{\rm comp})}{r_{\rm orb}}\right]^{1/2}. \tag{34}$$

The gravity of the companion star is also an important factor to alter solutions of the optically thick wind because it has the same effect as that the white dwarf mass has been increased by $M_{\rm comp}$ at the outer envelope. In our one-dimensional treatment, we assume the companion mass is uniformly distributed in a spherical shell between $r_{\rm orb} - R_{\rm comp}$ and $r_{\rm orb} + R_{\rm comp}$. The envelope is attracted by the gravity of the

TABLE 5

EFFECT OF COMPANION STAR

$M_{\rm WD}$ ($M_\odot$)	$M_{\rm comp}$ ($M_\odot$)	$r_{\rm cr}$ ($R_\odot$)	$L_{\rm drag}$ ($L_\odot$)	$L_{\rm ph}$ ($10^4\ L_\odot$)	log $T_{\rm ph}$ (K)	$r_{\rm ph}$ ($R_\odot$)	$v_{\rm wind,ph}$ (km s^{-1})	$r_{\rm orb}$ ($R_\odot$)	log $\rho_{\rm orb}$ (g cm^{-3})	$v_{\rm orb}$ (km s^{-1})	$C_{s,\rm orb}$ (km s^{-1})	$v_{\rm wind,orb}$ (km s^{-1})
0.6.....	...	0.35	...	1.626	4.423	6.04	317	...	...	...	...	...
0.6.....	0.1	0.35	34.9	1.637	4.355	8.31	205	0.545	−8.601	495	325	270
0.6.....	0.2	0.35	35.7	1.635	4.259	12.9	131	0.833	−9.085	428	246	358
0.8.....	...	0.50	...	2.273	4.299	12.7	353	...	...	...	...	...
0.8.....	0.2	0.50	98.6	2.291	4.207	19.4	226	0.897	−8.654	461	301	313
0.8.....	0.4	0.50	114	2.289	4.137	26.8	152	1.393	−9.105	405	223	369
1.0.....	...	0.65	...	2.898	4.182	24.5	361	...	...	...	...	...
1.0.....	0.2	0.65	218	2.958	4.135	30.7	256	0.954	−8.203	490	314	196
1.0.....	0.4	0.65	222	2.927	4.087	38.1	195	1.47	−8.821	427	255	360

mass, $M_{WD} + M_{comp}$, outside the companion orbit. Therefore, equations (1) and (5) has been modified to include the gravity of the companion star, i.e., M is replaced by M_{tot} which is equal to M_{WD} inside the radius of $r_{orb} - R_{comp}$ or equal to $M_{WD} + M_{comp}$ outside the radius of $r_{orb} + R_{comp}$. Between $r_{orb} - R_{comp}$ and $r_{orb} + R_{comp}$, M_{tot} is gradually increased in a way that the secondary is uniformly distributed within the spherical shell.

Thus, we have calculated six sequences of solutions for the various sets of white dwarf and companion star masses, i.e. $(M_{WD}, M_{comp}) = (0.6\ M_\odot, 0.1\ M_\odot)$, $(0.6\ M_\odot, 0.2\ M_\odot)$, $(0.8\ M_\odot, 0.2\ M_\odot)$, $(0.8\ M_\odot, 0.4\ M_\odot)$, $(1.0\ M_\odot, 0.2\ M_\odot)$, and $(1.0\ M_\odot, 0.4\ M_\odot)$. Figure 19 shows the structure of wind solutions with and without a companion for a 0.6 $M_\odot$ white dwarf. The chemical composition of the envelope are assumed to be the same as that in § 3. These solutions have a critical point at $r_{cr} = 0.35\ R_\odot$ and similar envelope masses of $2.33 \times 10^{-5}\ M_\odot$. The solution without a companion is denoted by the solid curves. Those with a 0.1 $M_\odot$ and with a 0.2 $M_\odot$ companion are denoted by dotted and dashed curves, respectively. The structure is hardly changed by the presence of a companion. It deviates from the structure without a companion only when the companion is rather massive and the uppermost part of the envelope is very extended.

Figure 20 shows the diffusive luminosity for the 0.6 $M_\odot$ white dwarf cases with and without a companion. The diffusive luminosity, L_r, hardly increases even for the 0.2 $M_\odot$ companion case, because the drag luminosity, L_{drag}, is as small as 0.22% of the total diffusive luminosity. (See also Table 5 for various physical values.) Such a small fraction of the drag luminosity stems from very low density of the envelope near the orbit. As shown in Figures 19 and 20 or Table 5, the companion orbit is outside the critical point. The matter is quickly accelerated near the critical point, and, as a result, the density drops sharply there. Therefore, the motion of the companion star is not able to generate large drag luminosity as can be easily understood from equation (27) or (31). The drag luminosity estimated by MacDonald et al. (1985), for example, is clearly an overestimation. The reason is that they assumed a static envelope around the white dwarf and did not include the response of the envelope to the energy input by the drag luminosity.

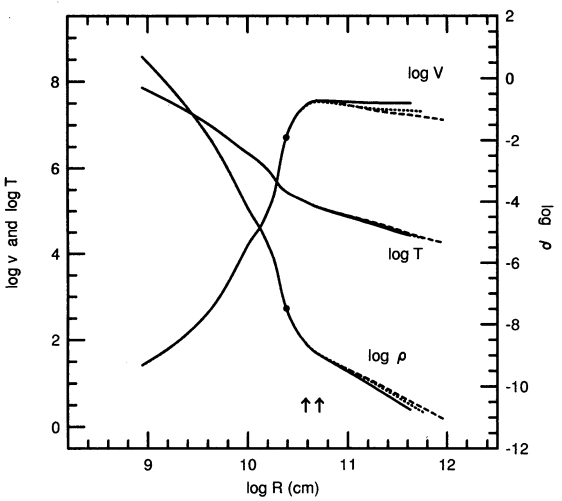

FIG. 19.—Wind velocity, the temperature, and the density are plotted against the radius for three mass-loss solutions of $M_{WD} = 0.6\ M_\odot$ and $r_{cr} = 0.35\ R_\odot$. The position of the critical point is denoted by a filled circle. Thick lines denote the envelope solutions without a companion star, dotted ones denote a 0.1 $M_\odot$ companion, and dashed ones denote a 0.2 $M_\odot$ companion. The position of the companion orbit is also denoted by an arrow. The left arrow denotes the position of the 0.1 $M_\odot$ companion.

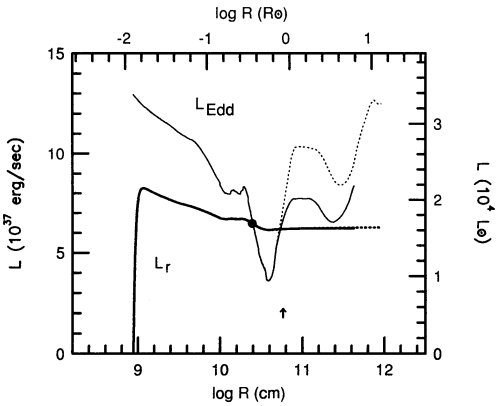

FIG. 20.—Diffusive luminosity, L_r, and the Eddington luminosity, $4\pi cGM_{tot}/\kappa$, are plotted against the radius for a 0.6 $M_\odot$ white dwarf. Solid curves denote the solutions without a companion star, and dashed ones denote those with a 0.2 $M_\odot$ companion. The position of the companion orbit is denoted by an arrow. The Eddington luminosity (*thin dotted curve*) increases around the position of the companion star. This is due to the contribution of the companion mass.

The presence of a companion increases the gravity outside the orbit and, as a result, the local Eddington luminosity goes up there. Therefore, even if the heat by drag is deposited at the orbit, this additional energy can easily escape from the envelope by diffusion and cannot be used to accelerate envelope matter. On the other hand, the gravity of the companion deepens the gravitational potential and the wind is decelerated. Figure 19 shows that the velocity is decreased a little by this effect especially for more massive companions.

Figure 21 shows the light curves for various white dwarf masses. The solid curves denote the solutions without a companion, that is, they are identical to the light curves in Figure 8. Dashed and dotted curves are the cases with a companion. Long-dashed lines correspond to a 0.1 $M_\odot$ companion star. Short-dashed lines denote a 0.2 $M_\odot$ and dotted ones a 0.4 $M_\odot$. For the 1.0 and 0.8 $M_\odot$ white dwarfs, we have examined two

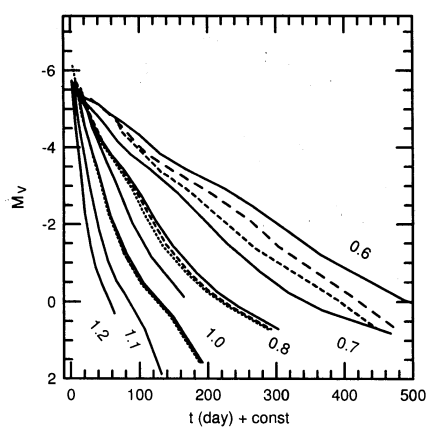

FIG. 21.—Theoretical light curves for various sets of the white dwarf and companion masses. Thick curves denote the solution without a companion (the same as in Fig. 8). Two other sequences are added each for $M_{WD} = 0.6$, 0.8, and 1.0 $M_\odot$ including the effects of companion star. The mass of the companion is assumed to be 0.1 $M_\odot$ (*long-dashed curve*), 0.2 $M_\odot$ (*short-dashed curve*), and 0.4 $M_\odot$ (*dotted curve*).

cases of the companion mass, i.e. 0.2 and 0.4 $M_\odot$. It is easily seen that these light curves are hardly changed by the presence of a companion star. Only for the 0.6 $M_\odot$ white dwarf, in which we have examined 0.1 and 0.2 $M_\odot$ companion, the slope of light curves becomes steeper and close to that of the 0.7 $M_\odot$ white dwarf.

The rate of decline in the light curves is affected by the change in the photospheric temperature even if the bolometric luminosity is constant. In the presence of a companion, the envelope must be extended in order to balance with stronger gravity compared with the case of no companion if the envelope mass is fixed. Then the surface temperature becomes lower in the case of more massive companion. Therefore, we obtain larger visual magnitude for more massive companion. This effect is stronger in earlier phase and becomes weaker in later phase so that we have a more rapid decline in the light curve of a more massive companion. However, the duration of nuclear burning, i.e. the evolutional timescale, is not changed by the presence of a companion, because the mass-loss rate is mainly determined near the critical point and, therefore, not changed in the presence of the companion.

6. DISCUSSIONS

6.1. *Dependence on Chemical Composition of Envelope*

We have assumed chemical composition of the envelope to be uniform with $X = 0.35$, $Y = 0.33$, $Z = 0.02$, C = 0.1, and O = 0.2 as a standard model. In this subsection we examine how the light curve depends on the chemical composition of the envelope. We change the values of X, Y, C, or O, but still assume the uniformity of the chemical composition in the envelope.

Figure 22 shows light curves of the decay phase for various sets of chemical composition. Thick and thin solid curves denote the light curves with the abundance of the standard model (i.e., $X = 0.35$, $Y = 0.33$, C = 0.1, and O = 0.2) as described above, but for various white dwarf masses. Various kinds of thick curves denote light curves of the 1.0 $M_\odot$ white dwarf but for various sets of chemical composition. Thick dotted and dashed curves correspond to (X, Y, C, O) = (0.35, 0.23, 0.2, 0.2) and (0.35, 0.13, 0.1, 0.4), respectively. These two curves have almost the same decline rate as the thick solid curve especially in early stage. Composition changes among helium, carbon, and oxygen causes only small (several percent) changes both in the opacity and the mean molecular weight. Therefore the envelope structure is not so changed and then the light curve itself depends weakly on the change of helium, carbon, and oxygen content.

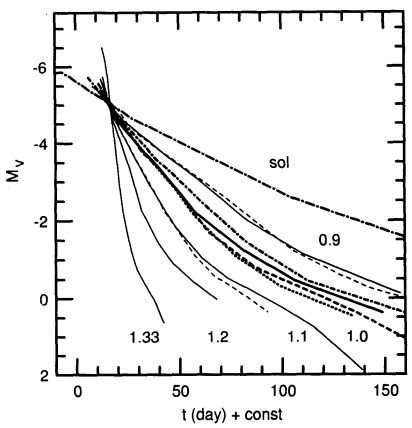

FIG. 22.—Theoretical light curves but for various sets of the chemical compositions. Thick type curves denote the light curves for 1.0 $M_\odot$ white dwarf. Thin type curves represent light curves for other white dwarf masses. Solid (thick and thin) curves denote the models with the standard chemical composition as mentioned in § 3 (the same as in Fig. 8). Thick dotted and dashed lines denote two other typical classical nova cases of (X, Y, C, O) = (0.35, 0.23, 0.20, 0.20) and (X, Y, C, O) = (0.35, 0.13, 0.10, 0.40) on a 1.0 $M_\odot$ white dwarf. Thick dot-dashed line denotes an extreme case of hydrogen-rich and no helium matter, i.e., (X, Y, C, O) = (0.70, 0.0, 0.1, 0.18) on a 1.0 $M_\odot$ white dwarf. Thin dashed lines denote neon novae of (X, Y, C, O, Ne) = (0.30, 0.2, 0.0, 0.3, 0.18) on 0.9 and 1.1 $M_\odot$ white dwarfs. Thick dot-long dashed lines denote the case of solar abundance, i.e., (X, Y, Z) = (0.70, 0.28, 0.02) on a 1.0 $M_\odot$ white dwarf.

Next we have checked the variation between helium and hydrogen content with fixed carbon and oxygen content. Using the opacity table of (0.70, 0.0, 0.1, 0.18), we have obtained an extreme case of hydrogen abundance. The results are plotted by the dot-dashed curve in Figure 22, which has a slightly slower decline rate than the above three cases. However, their difference is so small that these four curves have almost the same decline rates. The chemical composition of Nova Cygni 1978 has been estimated to be $X = 0.47$, $Y = 0.22$, and CNO = 0.3 from UV observation by Stickland et al. (1981). If the envelope has this composition, its theoretical light curve lies between the thick solid and the thick dot-dashed curves in Figure 22. Thus, even if we take into account the ambiguity of the chemical composition determination, we may conclude that our "standard curves" (solid curves for various white dwarf masses) will approximate the observed light curve of Nova Cygni 1978.

The envelope structure depends on the chemical composition through the opacity and the mean molecular weight. When the mass fractions of carbon, nitrogen, and oxygen are changed among them with the total amount of these three elements being fixed, the mean molecular weight slightly changes. As for the contributions of carbon, nitrogen, and oxygen to the opacity, are almost the same because they have successive atomic number and similar ionization energy levels. Therefore the opacity does not change so much if the total content of CNO elements is fixed. This is the reason why the light curves have almost the same decline rates. If helium is reduced and hydrogen is increased with the heavy elements being fixed, both the mass loss rate and the envelope mass decrease by the amount of 10%. These effects are canceled with each other in calculating the timescale of the decline phase of nova. As for the light curves, the photospheric temperature becomes smaller when hydrogen content is increased. This causes the increase in visual magnitude. But the bolometric luminosity decreases because the opacity increases. As a result, the resultant light curves are almost similar when the contents of heavy elements are fixed.

If the contents of carbon and oxygen are reduced equal to the solar value, i.e., 2%, we obtain light curves with very different decline rates. A thick dot-long dashed line denoted by sol in Figure 22 shows such a light curve of solar abundance, i.e., (X, Y, Z) = (0.7, 0.28, 0.02), on a 1.0 $M_\odot$ white dwarf. This kind of slow decline rate stems from a large envelope mass. If we compare two models having the same surface temperature but the different hydrogen content, the envelope mass of solar composition matter is much larger than that of CO-rich matter. This is because the temperature in the burning zone must be higher in order to generate the same nuclear energy as the case of CO-rich matter. Therefore, we obtain much slower light curves.

Further, we examine solutions for neon-rich material, which may be a model of neon novae. The abundance is assumed to be $X = 0.3$, $Y = 0.2$, $Z = 0.02$, C = 0.0, O = 0.3, and Ne = 0.18 by weight. We use an opacity table for this special composition calculated by F. J. Rogers & C. A. Iglesias (1993, private communication). The corresponding light curves are shown in Figure 22 for 0.9 and 1.1 $M_\odot$ white dwarfs (*thin dashed lines*). These light curves are almost the same as those of CO-rich materials.

To summarize, the differences in light curves are small if the total amount of CNO or CNO + Ne elements is larger than ~ 0.2. Therefore, even if they have a large ambiguity of the heavy element abundance, we can distinguish the difference of white dwarf mass by $\sim 0.05\ M_\odot$ as far as the CNO or CNO + Ne enriched novae are concerned. Roughly speaking, our light curve analysis has an accuracy of $0.05\ M_\odot$ in the determination of white dwarf mass.

6.2. *Acceleration outside the Photosphere*

We have neglected other acceleration mechanisms such as line-driven and dust-driven winds, which may occur outside the photosphere. These are not so important acceleration mechanisms compared with the optically thick wind, because the matter has been sufficiently accelerated deep inside the photosphere. Such an additional mechanism plays an important role only when the photon outside the photosphere has large momentum compared with that of the outflowing matter. However, the wind has much larger momentum than that of photon in most of our nova solutions. We show the ratio of the matter momentum to the photon momentum at the photosphere and less importance of the acceleration outside the photosphere.

Here we define the ratio of the matter momentum flux to the photon momentum flux at the photosphere as

$$\eta = \frac{\dot{M} v_{\rm ph}}{L_{\rm ph}/c} = 3\left(\frac{\dot{M}}{10^{21}\ {\rm g\ s^{-1}}}\right)\left(\frac{v_{\rm ph}}{10^{7}\ {\rm cm\ s^{-1}}}\right)\left(\frac{L_{\rm ph}}{10^{38}\ {\rm ergs\ s^{-1}}}\right)^{-1}. \tag{35}$$

The momentum flux ratio, η, of optically thick winds is evaluated at the photosphere as shown in Figure 23. The value of η is as large as 30 or more in early stages of nova and then decreases as the photospheric temperature increases. The reason of low values at low surface temperatures in the 0.6 and 0.5 $M_\odot$ sequences is due mainly to their low wind velocities. When η is larger than unity, we cannot expect effective acceleration outside the photosphere. It may work, however, when the optically thick wind almost stops and after that (i.e., from near point D to point A through point E in Fig. 1).

In optically thick winds, η increases much larger than unity whereas it cannot in line-driven winds. We briefly explain why η becomes much larger than unity. The maximum momentum flux that matter can get during its travel from r to $r + \Delta r$ is equal to the difference of pressure between r and $r + \Delta r$. In other words, when the matter get momentum from the photon momentum flux, its maximum value corresponds to the difference of radiation pressure between r and $r + \Delta r$. It is easily estimated from the diffusion equation, i.e.,

$$\Delta P_{\rm rad} = \frac{\tau L_r}{4\pi r^2 c}, \tag{36}$$

where we use the relation $\tau = \kappa\rho\,\Delta r$. Thus, the maximum momentum flux for entire spherical shell is equal to $\tau L_r/c$. We understand that the effective photon velocity decreases to c/τ by diffusion effect. In an optically thick and radiation dominant region, therefore, we estimate the maximum value of η as

$$\eta_{\rm max} = \frac{\tau L_r/c}{L_r/c} = \tau. \tag{37}$$

As shown in § 3, the acceleration of matter occurs at log T(K) $\sim$ 5.2. This acceleration region is deep inside the photosphere, i.e., at large τ region, in relatively early phase of novae. As the photospheric temperature increases close to log T(K) $\sim$ 5.2, the acceleration region approaches the photosphere, i.e., $\tau \sim 1$. Therefore, the momentum flux ratio becomes small and close to unity when log $T_{\rm ph}$(K) > 5.2.

The effective velocity in equation (37) is also derived from the random walk theory. The photon collides with matter $N = \tau^2$ times during its travel of interval D with optical depth τ ($\kappa\rho D = \tau$). As the photon walks Nl in total until it reaches the distance D. Here, l is the mean free path between collisions, i.e., $\kappa\rho l \sim 1$. So the effective velocity of photon is estimated to be $D/(Nl/c) = c/\tau$. When the effective velocity of photon decreases to c/τ, we regard that the photon momentum flux increases to $\tau L_r/c$. In other words, matter can get the momentum from photon through multiple collisions by much larger amount than that of the momentum flux of photon itself.

Thus, it is clear that in the optically thick wind radiation can impart momentum to matter much larger than that of the photon momentum flux at the photosphere.

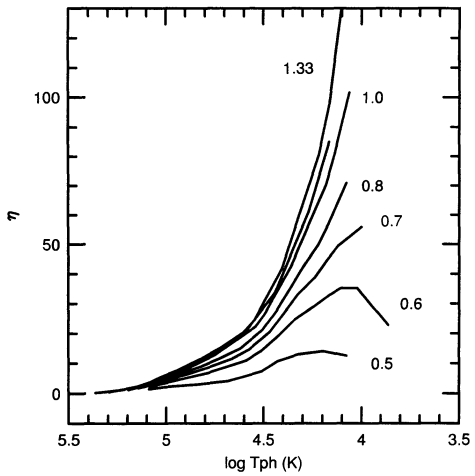

FIG. 23.—Ratio of matter momentum flux to photon momentum flux at the photosphere, η, is plotted against the photospheric temperature for various white dwarf masses. When η is larger than unity, we cannot expect effective acceleration outside the photosphere.

6.3. *Steady State Approximation*

Now we discuss the validity of steady state assumption. Many time-dependent calculations of shell flash on a white dwarf show that nuclear energy generation rate is very large just after the onset of nuclear burning, but gradually decreases and settles down to a constant rate, where the nuclear energy generation rate balances with the bolometric luminosity (Sparks, Starrfield, & Truran 1978; Iben 1982; Prialnik 1986; Prialnik & Kovetz 1992). This thermal equilibrium lasts until hydrogen burning vanishes (at point E in Fig. 1). One of the steady-state assumptions, equation (3), has been directly confirmed in the dynamical calculation by Prialnik (1986), where

the mass flux, $4\pi r^2 \rho v$, is almost constant throughout the envelope in the decay phase of nova.

We have examine whether or not our steady state solutions can reproduce Prialnik's results of 1.25 $M_\odot$ dynamical models. Here the chemical composition is assumed to be uniform with $X = 0.7$, $Y = 0.27$ and $Z = 0.03$ and we use the opacity formulae proposed by Iben (1975) and Stellingwerf (1975) which are based on the Los Alamos tables. Taking the same position of the critical point $r_{cr} = 3.4\ R_\odot$ as that of Prialnik's model, we obtain the almost identical physical values with those of Prialnik's dynamical models. We show such various physical values, as in the form of (the present model, Prialnik's), that $\log T_{cr}(\mathrm{K}) = (5.085, 5.053)$, $\log v_{ph}\ (\mathrm{cm\ s^{-1}}) = (6.89, 6.98)$, the mass above the critical point is $(1.1 \times 10^{-6}\ M_\odot, 1 \times 10^{-6}\ M_\odot)$, $\log r_{ph}\ (\mathrm{cm}) = (12.32, 12.40)$, and $\dot{M} = (1.24 \times 10^{-4}\ M_\odot\ \mathrm{yr^{-1}}, 1.26 \times 10^{-4}\ M_\odot\ \mathrm{yr^{-1}})$. These results show that our steady state solutions do reproduce Prialnik's model. The small difference between two results may originate from the differences in the opacities, the surface boundary conditions and other physical inputs.

A direct comparison between steady state models and time-dependent calculations has been done by Kato et al. (1989). They calculated one complete cycle of helium shell burning nova in two different ways, i.e., steady state approach and time-dependent calculation, using the same stellar parameters and physical inputs. Their two numerical results agrees very well with each other both in the evolutionary path of H-R diagram and in the interior structure such as the entropy distribution. Thus, we may conclude that our steady state approach is a good approximation to the decay phase of nova.

6.4. *Effects of Convective Energy Transfer*

We have neglected the convective energy transfer in the present work. In this subsection we discuss whether the convective energy transport is negligible or not. A part of the mass losing envelope becomes convectively unstable when the opacity decreases outward. Using the mixing length theory, we estimate how efficient is the convection in our solutions which are obtained without the convective energy transport. Here we assume that the ratio of the mixing length to the pressure scale height is 0.5. For example, the envelope model of 1.0 $M_\odot$ white dwarf with the critical point at $r_{cr} = 0.65\ R_\odot$, which is the same model as shown in Figure 2, has two convectively unstable regions: one is a wide region outside the iron peak and the other is a narrow one inside the iron peak.

The outer unstable region extends widely just outside the strong peak of the OPAL opacity between $\log T(\mathrm{K}) = 5.213$ and 4.253 (i.e., from $r = 1.17\ R_\odot$ to $18.6\ R_\odot$). In this region, however, the efficiency of convective energy transport is very small, because the density quickly drops as shown in Figure 4. The efficiency factor of convection (Henyey, Vardya, & Bodenheimer 1965),

$$\gamma = \frac{\nabla - \nabla'}{\nabla' - \nabla_{ad}}, \tag{38}$$

reaches the maximum value of 0.078 at the inner edge of this region (at $r = 1.17\ R_\odot$) and quickly drops to less than 0.01 at $r = 1.39\ R_\odot$ and $\log T(\mathrm{K}) = 5.126$. Here,

$$\nabla \equiv \frac{d \ln T}{d \ln P}, \tag{39}$$

and ∇' is the gradient describing the internal changes in convective bubbles as they move, and ∇_{ad} the adiabatic temperature gradient. This indicates that the convective motion can transport only a small part of the total energy due mainly to low density. So we expect that even if we include the convective energy transfer, it will not affect the structure.

The velocity of eddies is estimated based on the mixing length theory. The convective velocity reaches the maximum value of $v_{conv} = 70\ \mathrm{km\ s^{-1}}$ at the inner edge of the unstable region (at $r = 1.17\ R_\odot$) and decreases quickly to 1 km s^{-1} at $r = 1.67\ R_\odot$, and further to 0.1 km s^{-1} at $r = 1.81\ R_\odot$, where the wind velocity $v_{wind} = 300$–$360\ \mathrm{km\ s^{-1}}$ is much faster than the convective velocity. Even at the inner edge of the unstable region where the convection is most effective, it takes 2.28×10^3 s that eddies move to a half the pressure scale height, 0.23 $R_\odot$. On the other hand, this unstable region is carried out to $r = 2.16\ R_\odot$, where the efficiency of convection is already negligibly small (the efficiency factor cannot be obtained there because the structure is slightly superadiabatic). Therefore, we may conclude that eddies cannot turn over in such a supersonic outflowing envelope.

The inner unstable region appears between $\log T(\mathrm{K}) = 5.739$ and 6.303 (from $r = 0.225$ to $0.493\ R_\odot$). This is caused by a small peak in the opacity just inside the iron peak. In this region, the convective energy transport is effective but its region is very small. The efficiency factor itself is larger than 0.5 between $\log T(\mathrm{K}) = 6.293$ and 6.159 (from $r = 0.230$ to 0.287 $R_\odot$), and reaches the maximum value of 0.74. Such a small region of convection does not affect the entire structure of the envelope. For example, we have calculated a solution for a 1.1 $M_\odot$ white dwarf. If we assume the convective energy transport to be adiabatic in this region as an extreme case, the wind mass-loss rate increases 4.3% and the envelope mass also increases 4.1% for solutions with the same critical point, $r_{cr} = 0.5\ R_\odot$. This implies that if we compare these two sequences with and without the convection effect, the mass loss rate is almost the same between these two sequences for the same envelope mass. Therefore, the timescale of the light curves, $\Delta M/\dot{M}$, is not changed.

6.5. *Inner Boundary Condition*

We have adopted the inner boundary condition, equation (18), in which the nuclear luminosity L_n is estimated from the solutions calculated without nuclear energy generation. To check this assumption, we have replaced the integrated form of energy conservation equation (5) by the differential form,

$$\dot{M} T \frac{ds}{dM_r} = X \epsilon_H - \frac{dL_r}{dM_r}, \tag{40}$$

where s is the specific entropy, and obtained the new solutions. The boundary condition is set as

$$L_r = 0 \quad \text{at} \quad r = R_{WD}. \tag{41}$$

The new light curves thus obtained are shown in Figure 24 for three white dwarfs masses of 1.3, 1.0, and 0.7 $M_\odot$ as well as the light curves in Figure 8. The new light curves are almost identical with the old ones except in the upper part of the figure. The difference between the new and old envelope solutions are summarized as follows, for example, in the case of 1.0 $M_\odot$ white dwarf: For a solution with the critical point of $r_{cr} = 0.65\ R_\odot$, the wind mass loss rates are (eq. [18], eq. [41]) = $(7.20 \times 10^{21}, 6.95 \times 10^{21}\ \mathrm{g\ s^{-1}})$, and the envelope

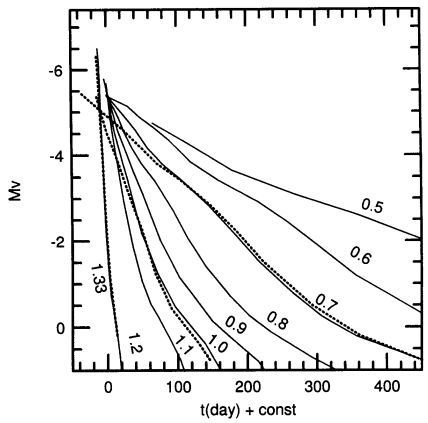

FIG. 24.—Same as for Fig. 8, but inner boundary condition (41) and differential form (40) are used to calculate the solutions. The solid curves are the same light curves as those in Fig. 8. The dashed curves denote the solutions calculated with eqs. (40) and (41).

masses are (9.46×10^{-6}, $1.15 \times 10^{-5}\ M_\odot$). For a solution with $r_{cr} = 0.2\ R_\odot$, the wind mass loss rates are (3.336×10^{20}, 3.378×10^{20} g s^{-1}), and the envelope mass (2.859×10^{-6}, $2.657 \times 10^{-6}\ M_\odot$). For the static solution at point D in Figure 1, the envelope masses are (1.807×10^{-6}, $1.702 \times 10^{-6}\ M_\odot$). As a result, the slope of the light curve becomes slower by 20%–30% at the upper part but slightly steeper in the lower part.

If we replace boundary condition (18) with (41), the temperature at the bottom of the envelope slightly changes. This is because the high temperature-dependence of nuclear energy generation rate; only a slight change in temperature at the burning zone is required to adjust the new boundary condition. The density increases in the burning region and, as a result, the envelope mass increases. These changes are restricted only in the nuclear burning region, and most part of the envelope remains unchanged. Therefore, the light curve is almost identical except for the very early phase, where the steady state assumption itself may break down.

Another problem for our inner boundary condition is related to equations (3) and (5), which come from the definition of the steady state (Eulerian steady state assumption). These equations result in nonzero velocity, nonzero wind mass-loss rate, and nonzero energy flow at the white dwarf surface. We cannot avoid this type of unphysical situation as long as Eulerian steady-state is concerned. If the mass-loss rate is small, however, this steady state approximation is good, because the bottom of the envelope is hydrostatic and the second term in the left hand side of equation (5) is small. When the mass-loss rate is large enough, however, the velocity at the bottom of the envelope is not so small and the inertia term in equation (1) and the second term in equation (5) cannot be neglected near the white dwarf surface (near the inner boundary). In this case, our steady state assumptions (Eulerian steady state) must be replaced with other type of definitions.

One possible way to avoid this difficulty has been proposed by Kato (1988), in which the equations are the same as those in Eulerian steady state in the upper part of the envelope, but approaches static equations at the bottom of the envelope. In this new definition of the steady state, the velocity and the mass-loss rate vanish at the bottom of the envelope. Kato (1988) confirmed that the solutions in this new steady state are essentially the same as those in the Eulerian steady state except that the velocity becomes zero at the white dwarf surface. This is because the bottom of the envelope is almost in a hydrostatic equilibrium, so that the zero-velocity solution has essentially the same structure as in the finite-velocity solution. Therefore, we can use the usual Eulerian steady state solutions as far as the mass loss rate is not so large. This Kato's new definition of steady state may be useful when the mass-loss rate is very large, i.e., just around the peak of the optical light curves.

7. CONCLUSIONS AND REMARKS

Under the assumption of steady-state, we have succeeded in constructing a sequence of steady state wind solutions which mimics a time-dependent evolution of the decay phase of novae, and have reproduced good quality light curves of novae. Comparison with a classical nova, Nova Cygni 1978, shows an excellent applicability of our theory. Our conclusions are summarized as follows:

1. Using the optically thick wind theory and the OPAL opacity, we have succeeded in reproducing good quality light curves in the decay phase of classical novae. The timescale of nova duration is drastically shortened by strong wind. The wind is driven by a strong iron peak of the OPAL opacity. This strong peak in the opacity is essentially important to reproduce a good quality light curves of novae. In other words, the optically thick winds are successful only when we use the OPAL capacity.

2. The optically thick wind occurs for white dwarfs more massive than 0.5 $M_\odot$, i.e., $M_{WD} \gtrsim 0.5\ M_\odot$. The wind phase lasts several months and the following static phase lasts a year for a 1.0 $M_\odot$ white dwarf. A significant part of the envelope mass is blown off during the wind phase. Even for a 0.6 $M_\odot$ white dwarf, the wind phase becomes as short as several years and the following static phase is shorter than 10 years. Thus, we have resolved a theoretical problem of nova duration: it has been argued that the theoretical nova duration, which is estimated to be $\sim 10^3$ yr from the nuclear burning period of the original envelope mass, is too long to agree with the observations (~ 10 yr).

3. A detailed case study of Nova Cygni 1978 shows a good agreement with the observational properties, i.e., the visual and ultraviolent light curves and the wind velocities of the decay phase of novae. This strongly supports the validity of our steady state approach and implies that optically thick winds really occur at least in the decay phase of novae.

4. Comparison of our theoretical light curves with the observational ones will provide a new way to determine the white dwarf mass and the distance to the star. The accuracy of mass determination may be less than 0.1 $M_\odot$ even if we include the ambiguity of chemical composition. Thus, if the mass of white dwarf is determined for many nova systems, it will be very useful for studies of novae and binary evolutions.

5. The drag luminosity in the common envelope phase is not so important either for the wind mass-loss rate or the light curves. The reason is that the companion orbit is placed outside the critical point (i.e., the main acceleration region of the wind) and the density drops sharply there. Since the drag luminosity depends linearly on the density, it drops to smaller than 1% of the photospheric luminosity. The mass-loss rate is determined mainly inside/near the critical point and, therefore, it is not affected by the presence of a companion star. The duration of nuclear burning is also not affected by the presence of a companion star. For relatively low-mass white dwarfs, the

decline rate of light curves is a little affected by the presence of a companion. For example, the decline rate of 0.6 $M_\odot$ white dwarf with a 0.2 $M_\odot$ companion is similar to that of 0.7 $M_\odot$ white dwarf without a companion. Thus, the accuracy of mass determination may be still within 0.1 $M_\odot$.

Our optically thick wind theory has succeeded in reproducing reasonable light curves of the decay phase of novae. Such good quality of light curves enables us to determine the mass of white dwarf and the distance to the star by fitting the theoretical light curves with the observational ones. This may be a powerful method for the mass determination of novae especially when the binary components are not known to us. If the masses of many nova systems are determined by this method, it will provide us unique information concerning the study of binary evolution.

For the white dwarf masses in nova systems, we have estimated in § 3.4 that Nova Cygni 1978 contains a 1.0 $M_\odot$ white dwarf. This value is much smaller than that of the "typical values" such as $\sim$1.2–1.3 $M_\odot$ for classical novae, which have been assumed in many theoretical works (e.g., Truran & Livio 1986; Prialnik 1986; Kato & Hachisu 1988, 1989) from the reason that such a short duration of nova is obtained only when the white dwarf mass is as large as 1.2–1.3 $M_\odot$. On the other hand, much less massive white dwarfs than the "typical values" are expected when we use the OPAL opacity because much stronger wind mass loss occurs even on less massive white dwarfs. Thus, we are forced to conclude that many nova systems contain much less massive white dwarfs such as $\leq$1.0 $M_\odot$ than has ever been considered. Further study and comparison with the observations are required in order to reach a definite conclusion, however.

From the theoretical point of view, we need the following observational data:

1. Light curves of the optical (y-magnitude is recommended) and the ultraviolet band for the same outburst. Infrared is also necessary to correctly estimate the UV emission;
2. Chemical abundance of the ejecta and its change during the outburst;
3. Mass of the ejecta.

These are compared with the values estimated from the optically thick wind theory and provides independent information to check the results of the light curve analysis.

We would like to thank F. J. Rogers and C. A. Iglesias for providing us new opacity tables for neon-rich material. We are also grateful to D. Prialnik for sending us her detailed numerical results. This work has been supported in part by the Grant-in-Aid for Scientific Research (04640272, 05242208, 05640314) of the Japanese Ministry of Education, Science, and Culture.

APPENDIX A

SURFACE BOUNDARY CONDITIONS AND OCCURRENCE OF WIND MASS LOSS

As mentioned in § 2, the usual surface boundary condition with the plane-parallel assumption is not appropriate because the mass-losing envelope has an extended structure near the surface region. In this appendix, we discuss what kind of surface boundary condition is reasonable for such an extended envelope with and without mass loss. Kato (1985) examined several kinds of boundary conditions and concluded that boundary conditions (12) and (13) are most appropriate for mass-losing envelopes. Here, we will examine the surface boundary condition in the same way as done by Kato (1985).

When the envelope is in hydrostatic equilibrium, we may solve

$$\frac{1}{\rho}\frac{dP}{dr}+\frac{GM}{r^2}=0\,, \tag{A1}$$

and equation (4) with L_r = constant instead of equations (1) and (3)–(5). Assuming that the opacity is a function only of temperature and that the mean molecular weight μ is constant, we can integrate these equations as

$$\rho=\frac{aT^3\mu m_a}{3kl_s}\left(F+\frac{C}{T^4}-l_s\right), \tag{A2}$$

$$P=\frac{aT^4}{3l_s}\left(F+\frac{C}{T^4}\right), \tag{A3}$$

where F and l_s are defined by

$$F\equiv\frac{4\kappa_{\rm ph}}{T^4}\int\frac{T^3}{\kappa}\,dT\,, \tag{A4}$$

$$l_s\equiv\left(\frac{L_r}{L_{\rm Edd}}\right)_{\rm ph}, \tag{A5}$$

and C is an integration constant. Substituting these relations into equation (4), we obtain

$$\frac{d\ln T}{d\ln r}=-\frac{\mu m_a GM\kappa}{4kT\kappa_{\rm ph}r}\left(F+\frac{C}{T^4}-l_s\right). \tag{A6}$$

This can be also integrated as

$$r=\frac{\mu m_a GM}{4kT}\frac{1}{H}\,, \tag{A7}$$

where

$$H \equiv \frac{\kappa_{\rm ph}}{T}\left\{\int \frac{dT}{\kappa[F+(C/T^4)-l_s]} + \text{constant}\right\}. \tag{A8}$$

Thus, all physical variables can be solved as a function of temperature only. Substituting equations (12), (15), and (A2) into (A6), we also obtain a relation at the photosphere, i.e.,

$$\left(\frac{d\ln T}{d\ln r}\right)_{\rm ph} = -\frac{3}{16}(\kappa\rho r)_{\rm ph}. \tag{A9}$$

We assume that the diffusion equation (4) is valid up to the photosphere. Then the photon flux from the blackbody, $4\pi r^2\sigma T^4$, should be greater than the diffusive flux L_r in the interior and equal to that at the photosphere. In other words, the temperature must be higher than the effective temperature, i.e.,

$$T \geq T_{\rm eff} \equiv \left(\frac{L_r}{4\pi r^2\sigma}\right)^{1/4}. \tag{A10}$$

In static envelopes the diffusive luminosity L_r is constant, therefore, this condition is equivalent with

$$\left(\frac{d\ln T}{d\ln r}\right)_{\rm ph} \leq -\frac{1}{2}, \tag{A11}$$

in the vicinity of the photosphere. Substituting this condition into equation (A9), we obtain a condition

$$(\kappa\rho r)_{\rm ph} \geq \tfrac{8}{3}. \tag{A12}$$

Therefore, we prove that $\tau = \kappa\rho r$ cannot become smaller than 8/3 at the photosphere. Correspondingly, the photospheric luminosity has an upper limit because we can derive a condition

$$l_s \leq l_s^{\rm max} \equiv F_{\rm ph} + \frac{C}{T_{\rm ph}^4} - \chi, \tag{A13}$$

from condition (A11) and equations (A6) and (16). This maximum photospheric luminosity depends clearly on the choice of the integration constant C, or in other words, depends on the definition of the photosphere.

To specify the integration constant C, we consider several surface boundary conditions. Here, we assume that the density distribution outside the photosphere is a power function of radius, i.e.,

$$\rho \propto r^{n_\rho}, \tag{A14}$$

and that the opacity κ is constant outside the photosphere. Then we consider the following three photospheric conditions, i.e.,

$$\tau_{\rm ph} = \int_{r_{\rm ph}}^{\infty} \kappa\rho\, dr = \frac{\kappa_{\rm ph}\rho_{\rm ph}r_{\rm ph}}{-1-n_\rho} = \frac{8}{3}, \tag{BC1}$$

$$\tau_{\rm ph} = r_{\rm ph}^2\int_{r_{\rm ph}}^{\infty} \kappa\rho r^{-2}\, dr = \frac{\kappa_{\rm ph}\rho_{\rm ph}r_{\rm ph}}{1-n_\rho} = \frac{2}{3}, \tag{BC2}$$

$$\tau_{\rm ph} = \int_{r_{\rm ph}}^{\infty} \kappa\rho\, dr = \frac{\kappa_{\rm ph}\rho_{\rm ph}r_{\rm ph}}{-1-n_\rho} = \frac{2}{3}, \tag{BC3}$$

Photospheric definition (BC1) is adopted in this paper and also in our previous papers to obtain the critical static solutions just after/before mass loss begins/stops. This comes from the condition that the static solution is smoothly connected to the wind solution where the density is decreasing with r^{-2} (the wind velocity is constant outside the photosphere). It is easily seen that when $l_s \to l_s^{\rm max}$, $n_\rho \to -2$ because $(\kappa\rho r)_{\rm ph} \to 8/3$ at $l_s \to l_s^{\rm max}$. Photospheric definition (BC2) with $n_\rho = -2$ was used by Ruggles & Bath (1979) for nova wind solutions and also by other authors mainly because spherical effect is taken into account. However, when $l_s \to l_s^{\rm max}$, $n_\rho \to -3$. This is not consistent with the wind solution of $n_\rho = -2$ at the junction of static/wind solutions. Photospheric definition (BC3) is the most popular one and has been used by many authors. This is also not consistent with the wind solutions at the junction because $n_\rho \to -5$, when $l_s \to l_s^{\rm max}$.

The density gradient n_ρ and the optical depth $\kappa\rho r$ at the photosphere are also rewritten as

$$n_\rho = \left(\frac{d\ln\rho}{d\ln r}\right)_{\rm ph} = \frac{1}{2\chi}\left(F_{\rm ph} + \frac{C}{T_{\rm ph}^4} + 3l_s - 4\right), \tag{A15}$$

$$\kappa_{\rm ph}\rho_{\rm ph}r_{\rm ph}=\frac{8}{3}\left(F_{\rm ph}+\frac{C}{T_{\rm ph}^4}-l_s\right)\frac{1}{\chi}. \tag{A16}$$

Substituting these equations into photospheric definitions (BC1)–(BC3), we obtain the integral constant C as follows:

$$\frac{C}{T_{\rm ph}^4}=-F_{\rm ph}+\frac{4-2\chi-l_s}{3}, \tag{A17}$$

$$\frac{C}{T_{\rm ph}^4}=-F_{\rm ph}+\frac{4+2\chi+5l_s}{9}, \tag{A18}$$

$$\frac{C}{T_{\rm ph}^4}=-F_{\rm ph}+\frac{4-2\chi+5l_s}{9}, \tag{A19}$$

for (BC1)–(BC3), respectively. Therefore, from equation (A13), we have obtained the maximum luminosity, i.e.,

$$l_s^{\rm max}=1-\tfrac{5}{4}\chi, \tag{A20}$$

$$l_s^{\rm max}=1-\tfrac{7}{4}\chi, \tag{A21}$$

$$l_s^{\rm max}=1-\tfrac{11}{4}\chi, \tag{A22}$$

for conditions (BC1)–(BC3), respectively. Equation (A20) is the same as equation (14), which is used to detect the junction of static/wind solutions in this paper. Substituting relations (A17)–(A19) into equation (A16), we obtain the photospheric optical depth defined by $\tau=\kappa\rho r$ as

$$\kappa_{\rm ph}\rho_{\rm ph}r_{\rm ph}=\frac{32}{9}\frac{1-l_s-\chi/2}{\chi}, \tag{A23}$$

$$\kappa_{\rm ph}\rho_{\rm ph}r_{\rm ph}=\frac{32}{27}\frac{1-l_s+\chi/2}{\chi}, \tag{A24}$$

$$\kappa_{\rm ph}\rho_{\rm ph}r_{\rm ph}=\frac{32}{27}\frac{1-l_s-\chi/2}{\chi}, \tag{A25}$$

for conditions (BC1)–(BC3), respectively. It is easily seen that when $l_s\rightarrow l_s^{\rm max}$, $\kappa\rho r$ at the photosphere becomes 8/3.

We consider one more example, i.e., the plane-parallel approximation, where we solve

$$\frac{1}{\rho}\frac{dP}{dr}+\frac{GM}{R^2}=0, \tag{A26}$$

$$\frac{dT}{dr}=-\frac{3\kappa\rho L_r}{16\pi acT^3R^2}, \tag{A27}$$

instead of equations (A1) and (4). Here R is the radius of the star. We assume that the opacity κ is constant outside the photosphere. Then, we can integrate equation (A26) as

$$P(\tau)=P(\tau=0)+\frac{GM}{\kappa R^2}\tau. \tag{A28}$$

Substituting a relation calculated by Nomoto & Sugimoto (1974) on the plane-parallel photosphere, i.e.,

$$P(\tau=0)=\tfrac{1}{2}P_{\rm rad}(\tau=\tfrac{2}{3})=\tfrac{1}{2}\,\tfrac{1}{3}aT_{\rm ph}^4, \tag{BC4}$$

into equation (28), we have

$$P_{\rm ph}\equiv P\left(\tau=\frac{2}{3}\right)=\frac{1}{6}aT_{\rm ph}^4+\frac{2}{3}\frac{GM}{\kappa R^2}, \tag{A29}$$

where $P_{\rm rad}$ denotes the radiation pressure. Equating two relations (A3) and (A29), we obtain the integral constant C as

$$\frac{C}{T_{\rm ph}^4}=-F_{\rm ph}+\frac{1+l_s}{2}, \tag{A30}$$

for the plane-parallel condition (BC4). Then the maximum luminosity and the photospheric optical depth are written as

$$l_s^{\rm max}=1-2\chi, \tag{A31}$$

TABLE A1

SURFACE BOUNDARY CONDITIONS

Boundary Conditions	$\frac{C}{T_{ph}^4}$	$\kappa_{ph}\rho_{ph}r_{rph}$	$\kappa_{ph}\rho_{ph}r_{ph}(l_s^{max})$	V_{ph}	$V_{ph}(l_s^{max})$	l_s^{max}
BC1	$-F_{ph}+\frac{4-2\chi-l_s}{3}$	$\frac{32}{9}\frac{1-l_s-\chi/2}{\chi}$	$\frac{8}{3}$	$\frac{4(2-\chi-2l_s)}{\chi(4-2\chi-l_s)}$	$\frac{2}{1-\chi/4}$	$1-\frac{5}{4}\chi$
BC2	$-F_{ph}+\frac{4+2\chi+5l_s}{9}$	$\frac{32}{27}\frac{1-l_s+\chi/2}{\chi}$	$\frac{8}{3}$	$\frac{4(2-2l_s+\chi)}{\chi(4+5l_s+2\chi)}$	$\frac{2}{1-3\chi/4}$	$1-\frac{7}{4}\chi$
BC3	$-F_{ph}+\frac{4-2\chi+5l_s}{9}$	$\frac{32}{27}\frac{1-l_s-\chi/2}{\chi}$	$\frac{8}{3}$	$\frac{4(2-2l_s-\chi)}{\chi(4+5l_s-2\chi)}$	$\frac{2}{1-7\chi/4}$	$1-\frac{11}{4}\chi$
BC4	$-F_{ph}+\frac{1+l_s}{2}$	$\frac{4(1-l_s)}{3\chi}$	$\frac{8}{3}$	$\frac{2(1-l_s)}{\chi(1+l_s)}$	$\frac{2}{1-\chi}$	$1-2\chi$

$$\kappa_{ph}\rho_{ph}r_{ph}=\frac{4}{3}\frac{1-l_s}{\chi}. \tag{A32}$$

Other various surface values for these different definitions of the photosphere are summarized in Table A1.

When the luminosity is equal to the maximum luminosity, these four definitions of photosphere converge into the same condition, i.e., $(d\ln T/d\ln r)=-1/2$, and $\kappa\rho r=8/3$ at $r=r_{ph}$. The only difference is the numerical value of l_s^{max}, which is very close to the unity as shown in equations (A20)–(A22) and (A31) or in the last column of Table A1. The value of χ are as small as $\sim 10^{-3}$ for typical nova solutions so that the critical static solutions with the maximum luminosity is almost the same among these four different photospheric conditions. As a result, the structure can be determined almost independently of the photospheric conditions of (BC1)–(BC4).

The occurrence of wind mass loss can be detected by the condition of $l_s=l_s^{max}$. If the luminosity coming from deep inside the photosphere is less than the maximum value, i.e., $l_s<l_s^{max}$, a static solution exists. When the luminosity exceed this value, static solutions are replaced by wind solutions. The transition from static to wind solution occurs smoothly because these two critical solutions have very similar structures.

The structure of the envelope changes from plane-parallel to spherical before the wind mass loss occurs as mentioned in § 2.4. When the luminosity is small compared with the Eddington luminosity, the static solution has a plane-parallel structure. The luminosity goes up close to the Eddington value, the surface structure changes from plane-paarallel to spherical. A critical point appears near the photosphere when steady mass loss occurs. As the luminosity deep inside the photosphere becomes large, the wind mass-loss rate increases and the critical point moves inward relative to the photosphere.

This structure change can be well understood in terms of the homology invariant $V=GM\rho/rP$, the ratio of the thermal energy to the gravitational energy. In the theory of stellar structures it is one of the popular characteristic properties that V becomes as small as 2 in extended spherical structures (Hayashi, Hoshi, & Sugimoto 1962). When the luminosity is small, the envelope around the white dwarf is thin. Then, V is large as seen from Table A1 because χ depends weakly on T and is always small compared with the unity. As the luminosity increases, V_{ph} decreases to ~ 2. This can be understood from

$$V=\frac{GM\rho}{rP}=\frac{3}{4}\frac{\tau L_{Edd}}{L}, \tag{A33}$$

here we use equations (12) and (15) and $\tau=\kappa\rho r$. For the critical static solution, $\tau=8/3$, (A33) becomes

$$V=2\frac{L_{Edd}}{L}. \tag{A34}$$

Therefore, V is very close to 2 at the junction of static/wind solutions. On the other hand, V_{ph} is also close to 2 for steady mass-loss solutions. This is because we adopt the surface boundary condition of $\tau=2.7$. If we use a different boundary condition like $\tau\sim 1000$, for example, the surface region should have plane-parallel structure and be inconsistent with wind solutions. These properties support that our definition of the photosphere is reasonable and useful to detect the junction of static/wind solutions, that is, τ must be as small as 8/3 at the photosphere for extended envelopes both for static/wind solutions.

APPENDIX B

NUMERICAL TECHNIQUES

A trapezoidal implicit method is used to integrate the basic equations. This method is rather different from popular Runge-Kutta method used by many other people such as Ruggles & Bath (1979). So that we briefly explain our numerical method for obtaining wind solutions.

For simplicity, we rewrite the basic equations as follows:

$$\frac{dy_1}{dx} = f_1(y_1, y_2, x)\,, \tag{B1}$$

$$\frac{dy_2}{dx} = f_2(y_1, y_2, x)\,, \tag{B2}$$

where

$$x = \log r\,, \tag{B3}$$

$$y_1 = \log T\,, \tag{B4}$$

$$y_2 = \log v\,, \tag{B5}$$

$$f_1 = \frac{d\log T}{d\log r} = -\frac{3\kappa\rho L_r}{16\pi acrT^4}\,, \tag{B6}$$

$$f_2 = \frac{\mathrm{d}\log v}{d\log r} = \left[\frac{2kT}{\mu m_a} - \frac{GM}{r} + \left(\frac{k\rho}{\mu m_a} + \frac{4aT^3}{3}\right)\frac{3\kappa L_r}{16\pi acrT^3}\right]\Big/\left(v^2 - \frac{kT}{\mu m_a}\right). \tag{B7}$$

It is noted that the density ρ is a function of v and r as seen from equation (3).

Then, the trapezoidal implicit is written as

$$y_1(x+\Delta x) = y_1(x) + \tfrac{1}{2}\Delta x\{f_1[y_1(x), y_2(x), x] + f_1[y_1(x+\Delta x), y_2(x+\Delta x), x+\Delta x]\}\,, \tag{B8}$$

$$y_2(x+\Delta x) = y_2(x) + \tfrac{1}{2}\Delta x\{f_2[y_1(x), y_2(x), x] + f_2[y_1(x+\Delta x), y_2(x+\Delta x), x+\Delta x]\}\,. \tag{B9}$$

If we assume a set of trial values y_1^0 and y_2^0, the differences from the true values, i.e.,

$$\delta y_1 = y_1(x+\Delta x) - y_1^0\,, \tag{B10}$$

$$\delta y_2 = y_2(x+\Delta x) - y_2^0\,, \tag{B11}$$

can be estimated from

$$\delta y_1 = \frac{1}{\det A}\begin{vmatrix} U_1 & A_{12} \\ U_2 & A_{22}\end{vmatrix}\,, \tag{B12}$$

$$\delta y_2 = \frac{1}{\det A}\begin{vmatrix} A_{11} & U_1 \\ A_{21} & U_2\end{vmatrix}\,, \tag{B13}$$

where

$$A_{11} = \frac{1}{2}\frac{\partial f_1(y_1^0, y_2^0, x+\Delta x)}{\partial y_1}\Delta x - 1\,, \tag{B14}$$

$$A_{12} = \frac{1}{2}\frac{\partial f_1(y_1^0, y_2^0, x+\Delta x)}{\partial y_2}\Delta x\,, \tag{B15}$$

$$A_{21} = \frac{1}{2}\frac{\partial f_2(y_1^0, y_2^0, x+\Delta x)}{\partial y_1}\Delta x\,, \tag{B16}$$

$$A_{22} = \frac{1}{2}\frac{\partial f_2(y_1^0, y_2^0, x+\Delta x)}{\partial y_2}\Delta x - 1\,, \tag{B17}$$

$$U_1 = y_1^0 - y_1(x) - \tfrac{1}{2}\{f_1[y_1(x), y_2(x), x] + f_1(y_1^0, y_2^0, x+\Delta x)\}\Delta x\,, \tag{B18}$$

$$U_2 = y_2^0 - y_2(x) - \tfrac{1}{2}\{f_2[y_1(x), y_2(x), x] + f_2(y_1^0, y_2^0, x+\Delta x)\}\Delta x\,, \tag{B19}$$

$$\det A = \begin{vmatrix} A_{11} & A_{12} \\ A_{21} & A_{22}\end{vmatrix}\,. \tag{B20}$$

We start the iteration by asuming trial values of y_1^0 and y_2^0, and repeat the iteration until $|\delta y/\Delta x|$ becomes smaller than 10^{-7}. Usually it takes several cycles. Here we fix the mean molecular weight μ during the iteration. Therefore, we use the following formula:

$$\frac{\partial f_1}{\partial y_1} = \ln 10 \times f_1 \times \left(\frac{\partial \ln \kappa}{\partial \ln T} + \frac{\partial \ln L_r}{\partial \ln T} - 4\right), \tag{B21}$$

$$\frac{\partial f_1}{\partial y_2} = \ln 10 \times f_1 \times \left(\frac{\partial \ln \kappa}{\partial \ln v} + \frac{\partial \ln L_r}{\partial \ln v} - 1\right), \tag{B22}$$

$$\frac{\partial f_2}{\partial y_1} = \ln 10 \times f_2 \times \frac{-kT/\mu m_a}{v^2 - kT/\mu m_a} + \frac{\ln 10}{v^2 - kT/\mu m_a}\left[\frac{2kT}{\mu m_a} + 4aT^3 \frac{3\kappa L_r}{16\pi acrT^3} + \left(\frac{k\rho}{\mu m_a} + \frac{4aT^3}{3}\right)\frac{3\kappa L_r}{16\pi acrT^3}\left(\frac{\partial \ln \kappa}{\partial \ln T} + \frac{\partial \ln L_r}{\partial \ln T} - 3\right)\right], \tag{B23}$$

$$\frac{\partial f_2}{\partial y_2} = \ln 10 \times f_2 \times \frac{-2v^2}{v^2 - kT/\mu m_a} + \frac{\ln 10}{v^2 - kT/\mu m_a}\left[-\frac{k\rho}{\mu m_a}\frac{3\kappa L_r}{16\pi acrT^3} + \left(\frac{k\rho}{\mu m_a} + \frac{4aT^3}{3}\right)\frac{3\kappa L_r}{16\pi acrT^3}\left(\frac{\partial \ln \kappa}{\partial \ln v} + \frac{\partial \ln L_r}{\partial \ln v}\right)\right], \tag{B24}$$

and

$$\frac{\partial \ln L_r}{\partial \ln T} = -\frac{\dot{M}}{L_r}\left(\frac{5}{2}\frac{kT}{\mu m_a} + \frac{16}{3}\frac{aT^4}{\rho}\right), \tag{B25}$$

$$\frac{\partial \ln L_r}{\partial \ln v} = -\frac{\dot{M}}{L_r}\left(v^2 + \frac{4aT^4}{3\rho}\right), \tag{B26}$$

$$\frac{\partial \ln \kappa}{\partial \ln v} = -\frac{\partial \ln \kappa}{\partial \ln \rho}. \tag{B27}$$

The partial derivatives $(\partial \ln \kappa/\partial \ln T)_\rho$ and $(\partial \ln \kappa/\partial \ln \rho)_T$ are calculated from the opacity tables.

Usually we start the calculation from a vicinity of the critical point assuming rough initial values. Fortunately,the trapezoidal implicit method converges even if we start the calculation from a very rough estimation of f_2.

The mesh number we have used is typically several hundreds for the region upper to the critical point. We use 2000 meshes for the region lower to the critical point. The total number of mesh points may be reduced to several hundreds if an enough number of mesh points are allotted to the regions where the physical variables change quickly, that is, near the opacity peak and the photosphere.

When the wind mass loss rate is relatively low, i.e., $\dot{M} = 10^{-6}$–$10^{-7}\ M_\odot\ \mathrm{yr}^{-1}$, we can obtain the solution even if we use the Runge–Kutta method. However, the Runge–Kutta method breaks down when the wind mass-loss rate increases to $\dot{M} \sim 10^{-5}\ M_\odot\ \mathrm{yr}^{-1}$ or more. It usually fails to follow the transonic solution at the first integral step from the critical point. The solution sometimes migrates from the transonic solution to the other type of solution, i.e., the subsonic solutions which are the solutions of the same basic equations. Therefore, even minute deviations in the trial values of $y_1^0 = \log T^0$ and $y_2^0 = \log v^0$ from the true value result in large deviations of the solution at a little outside/inside the critical point when we use the Runge-Kutta method.

Another type of difficulty appears as the mass-loss rate increases. In order to obtain the solution which satisfies surface boundary conditions (12) and (13), we must specify the value of the density at the critical point with very high accuracy. For example, we need at least eight digits of the density value, i.e., its relative accuracy reaches $\sim 10^{-8}$ for $\dot{M} \sim 10^{-5}\ M_\odot\ \mathrm{yr}^{-1}$. Much more accuracy is needed for higher mass-loss rates. The same kind of situation appears when we directly integrate stellar structures starting from the center of the star. If we take a set of trial values at the center, we experience that the solution diverges near the photosphere. To obtain the solution which satisfies the surface boundary conditions in such a situation we need the same order of high accuracy as wind mass-loss solutions.

Finally we show an example of numerical integration for the readers who want to follow our method. It is an envelope solution on a 1.0 $M_\odot$ white dwarf, which is the same one as in Figures 2 and 3 (*thick solid curve*). This solution has the density of $\rho_{cr} = 2.4674537 \times 10^{-8}\ \mathrm{g\ cm}^{-3}$, the temperature of $\log T_{cr}(\mathrm{K}) = 5.5163$, the diffusive luminosity of $L_r = 1.560 \times 10^{38}\ \mathrm{ergs\ s}^{-1}$ at the critical point $r_{cr} = 0.2\ R_\odot$, i.e., $\log r_{cr}\ (\mathrm{cm}) = 10.14364$. We start the calculation from a point which deviates from the critical point by

TABLE B1

EXAMPLE OF WIND SOLUTION[a]

Position	$\log r$ (cm)	$\log \rho$ (g cm^{-3})	$\log T$ (K)	$\log v$ (cm s^{-1})	$\log L_r$ (ergs s^{-1})	$\kappa\rho r$	κ (cm^2 s^{-1})
Photosphere.....	10.651	−9.790	5.007	7.912	38.182	2.71	0.373
Critical point.....	10.144	−7.6077509	5.5163	6.744	38.193	1.09×10^2	0.316
Bottom	8.7326	0.660	7.956	1.298	38.256	5.48×10^8	0.222

[a] The wind mass-loss rate is $\dot{M} = 3.336 \times 10^{20}\ \mathrm{g\ s}^{-1}$ and the envelope mass is $\Delta M = 5.69 \times 10^{27}$ g for this example.

$\Delta \log r = 0.001$ with initial guesses of $(d \log T/d \log r) = -1.98$ and $(d \log v/d \log r) = 9.16$ for the region above the critical point but $(d \log v/d \log r) = 13.1$ for the region below the critical point. The corresponding photospheric values are $\log T_{\rm ph}$ (K) = 5.007, $\log r_{\rm ph}$ (cm) = 10.651, $L_{\rm ph} = 1.52 \times 10^{38}$ ergs s^{-1}, $\log v_{\rm ph}$ (cm s^{-1}) = 7.912. At the bottom of the envelope, $\log T$(K) = 7.956, $\log \rho$ (g cm^{-3}) = 0.660, $\log v$ (cm s^{-1}) = 1.298, $\log P$ (dyn cm^{2}) = 17.317 at $\log r$ (cm) = 8.7326. The mass-loss rate is $\dot{M} = 3.336 \times 10^{20}$ g s^{-1} and the envelope mass is $\Delta M = 5.69 \times 10^{27}$ g, i.e., $\Delta M = 2.51 \times 10^{23}$ g above the critical point and $\Delta M = 5.69 \times 10^{27}$ g below the critical point. Various physical values are also tabulated in Table B1. You may use these values to examine whether your code is correct or not.

REFERENCES

Bodenheimer, P., & Taam, R. E. 1984, ApJ, 280, 771
Bondi, H. 1952, MNRAS, 112, 195
Cox, A. N., King, D. S., & Tabor, J. E. 1973, ApJ, 172, 423
Cox, A. N., & Stewart, J. 1970a, ApJS, 19, 243
———. 1970b, ApJS, 19, 261
Duerbeck, H. W., Rindermann, K., & Seitter, W. C. 1980, A&A, 81, 157
Eggleton, P. P. 1983, ApJ, 268, 368
Finzi, A., & Wolf, R. A. 1971, A&A, 11, 418
Friedjung, M. 1966, MNRAS, 132, 317
Gallagher, J. S., Kaler, J. B., Olson, E. C., Hartkopf, W. I., & Hunter, D. A. 1980, PASP, 92, 46
Gallagher, J. S., & Starrfield, S. 1978, ARA&A, 16, 171
Henyey, L., Vardya, M. S., & Bodenheimer, P. 1965, ApJ, 142, 841
Hayashi, C., Hoshi, R., & Sugimoto, D. 1962, Prog. Theor. Phys. Suppl., 22, 1
Iben, I., Jr. 1975, ApJ, 196, 525
———. 1982, ApJ, 259, 244
Iglesias, C. A., & Rogers, F. J. 1991, ApJ, 371, L73
———. 1993, ApJ, 412, 752
Iglesias, C. A., Rogers, F. J., & Wilson, B. G. 1987, ApJ, 322, L45
———. 1990, ApJ, 360, 221
Kaler, J. B. 1986, PASP, 98, 243
Kato, M. 1983a, PASJ, 35, 33
———. 1983b, PASJ, 35, 507
———. 1985, PASJ, 37, 19
———. 1988, in Lecture Notes in Physics, Vol. 305, Atmospheric Diagnostics of Stellar Evolution, ed. K. Nomoto (Berlin: Springer), 156
———. 1990a, ApJ, 355, 277
———. 1990b, ApJ, 362, L17
———. 1991, ApJ, 369, 471
———. 1994, A&A, 281, L49
Kato, M., & Hachisu, I. 1988, ApJ, 329, 808
———. 1989, ApJ, 346, 424
———. 1991a, ApJ, 373, 620
———. 1991b, ApJ, 383, 761
———. 1994, MNRAS, submitted
Kato, M., & Iben, I. 1992, ApJ, 394, L47
Kato, M., Saio, H., & Hachisu, I. 1989, ApJ, 340, 509
Livio, M., Shankar, A., Burkert, A., & Truran, J. W. 1990, ApJ, 356, 250
Livio, M., & Soker, N. 1988, ApJ, 329, 764
MacDonald, J. 1980, MNRAS, 191, 933
MacDonald, J., Fujimoto, M. Y., & Truran, J. W. 1985, ApJ, 294, 263
Nariai, K., Nomoto, K., & Sugimoto, D. 1980, PASJ, 32, 473
Nomoto, K., & Sugimoto, D. 1974, PASJ, 26, 129
Nomoto, K., Thielemann, F., & Yokoi, K. 1984, ApJ, 286, 644
Paczyński, B., & Prószyński, M. 1986, ApJ, 302, 519
Payne-Gaposchkin, C. 1957, The Galactic Novae (Amsterdam: North-Holland)
Patterson, J. 1984, ApJS, 54, 443
Prialnik, D. 1986, ApJ, 310, 222
Prialnik, D., & Kovetz, A. 1992, ApJ, 385, 665
Prialnik, D., Shara, M. M., & Shaviv, G. 1978, A&A, 62, 339
Quinn, T., & Paczyński, B. 1985, ApJ, 289, 634
Ritter, H., Politano, M., Livio, M., & Webbink, R. F. 1991, ApJ, 376, 177
Rogers, F. J., & Iglesias, C. A. 1992, ApJS, 79, 507
Ruggles, C. L. N., & Bath, G. T. 1979, A&A, 80, 97
Seitter, W. C. 1990, in Physics of Classical Novae, ed. A. Cassetella & R. Viotti (Berlin: Springer), 79
Shankar, A., Livio, M., & Truran, J. 1991, ApJ, 374, 623
Shima, E., Matsuda, T., Takeda, H., & Sawada, K. 1985, MNRAS, 217, 367
Sparks, W. N., Starrfield, S., & Truran, J. W. 1978, ApJ, 220, 1063
Starrfield, S. 1989, in Classical Novae, ed. M. F. Bode & A. Evans (New York: Wiley), 39
Stellingwerf, R. F. 1975, ApJ, 195, 441; 199, 705
Stickland, D. J., Penn, C. J., Seaton, M. J., Snijders, M. A. J., & Storey, P. J. 1981, MNRAS, 197, 107
Taam, R. E., & Bodenheimer, P. 1989, ApJ, 337, 849
Truran, J. W., & Livio, M. 1986, ApJ, 308, 721
Weidemann, V. 1990, ARA&A, 28, 103
Żytkow, A. 1972, Acta Astron., 22, 103
———. 1973, Acta Astron., 23, 121